Time domain ptychography

by

Dirk-Mathys Spangenberg

Dissertation presented for the degree of Doctorate of Philosophy in Physics in the Faculty of Science at Stellenbosch University

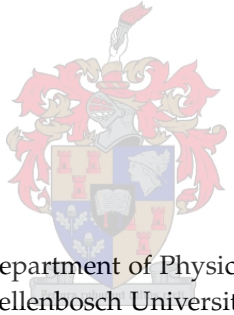

Department of Physics,
Stellenbosch University,
Private Bag X1, Matieland 7602, South Africa.

Promoters:

Prof. E.G. Rohwer	Dr. P.H. Neethling	Prof. A. Forbes
Department of Physics	Department of Physics	CSIR-NLC
Stellenbosch University	Stellenbosch University	Stellenbosch University

March 2015

Declaration

By submitting this dissertation electronically, I declare that the entirety of the work contained therein is my own, original work, that I am the sole author thereof (save to the extent explicitly otherwise stated), that reproduction and publication thereof by Stellenbosch University will not infringe any third party rights and that I have not previously in its entirety or in part submitted it for obtaining any qualification.

Date: .....

Abstract

Time domain ptychography

D. Spangenberg

Department of Physics,
Stellenbosch University,
Private Bag X1, Matieland 7602, South Africa.

Dissertation: PhD

January 2015

In this work we investigate a new method to measure the electric field of ultrafast laser pulses by extending a known measurement technique, ptychography, in the spatial domain to the time domain which we call time domain ptychography. The technique requires the measurement of intensity spectra at different time delays of an unknown temporal object and a known probe pulse. We show for the first time by measurement and calculation that this technique can be applied with excellent results to recover both the amplitude and phase of a temporal object. This technique has several advantages, such as fast convergence, the resolution is limited by the usable measured spectral bandwidth and the recovered phase has no sign ambiguity. We then extend the technique to pulse characterization where the probe is derived form the temporal object by filtering meaning the probe pulse is also unknown, but the spectrum of the probe pulse must be the same as the spectrum of the temporal object before filtering. We modify the reconstruction algorithm, now called ptychographic iterative reconstruction algorithm for time domain pulses (PIRANA), in order to also reconstruct the probe and we show for the first time that temporal objects, a.k.a laser pulses, can be reconstructed with this new modality.

Uittreksel

Tyd gebieds tigografie

("Time domain ptychography")

D. Spangenberg

Departement Fisika,
Stellenbosch Universiteit,
Privaatsak X1, Matieland 7602, Suid Afrika.

Proefskrif: PhD

Januarie 2015

In hierdie werk het ons 'n nuwe metode ondersoek om die elektriese veld van 'n ultravinnige laser puls te meet deur 'n bekende meettegniek wat gebruik word in die ruimtelike gebied, tigografie, aan te pas vir gebruik in die tyd gebied genaamd tyd gebied tigografie. Die tegniek vereis die meting van 'n reeks intensiteit spektra by verskillende tyd intervalle van 'n onbekende 'tyd voorwerp' en 'n bekende monster puls. Ons wys vir die eerste keer deur meting en numeriese berekening dat hierdie tegniek toegepas kan word met uitstekende resultate, om die amplitude en fase van 'n 'tyd voorwerp' te meet. Hierdie tegniek het verskeie voordele, die iteratiewe proses is vinnig, die resolusie van die tegniek word bepaal deur die spektrale bandwydte gemeet en die fase van die 'tyd voorwerp' word met die korrekte teken gerekonstrueer. Ons het hierdie tegniek uitgebrei na puls karakterisering waar die monster pulse afgelei word, deur 'n bekende filter te gebruik, van die onbekende 'tyd voorwerp' nl. die inset puls. Ons het die iteratiewe algoritme wat die 'tyd voorwerp' rekonstrueer aangepas om ook die monster puls te vind en ons wys dat ons hierdie metode suksesvol kan gebruik om laser pulse te karakteriseer.

Acknowledgements

I would like to express my sincere gratitude to the following people and organisations:
Thomas Feurer, with whom I had the great privilege to work with closely and whose input in this work was invaluable.
Erich Rohwer and Pieter Neethling for fantastic guidance and support, whose outlook in the framework of team effort and enablement allowed for many opportunities to be realised.
Andrew Forbes for support and the opportunity to have done experimental work with him and members of his group at the CSIR as well as the exposure to the research environment at the CSIR-NLC.
Angela Dudley for her time and help in the work done at the CSIR-NLC.
The NRF, NLC and the faculty of science for funding during my studies.

Dedications

Hierdie tesis word opgedra aan: eerstens my familie, dan die element Boron asook uiteindelik die simbool κ

Contents

List of Figures

List of Tables

Nomenclature

Constants

c =	$2.9979 \times 10^8\,\mathrm{m/s}$
i =	$\sqrt{-1}$

Variables

ω	Angular frequency
ω_0	Carrier frequency

Vectors and Tensors

$\mathbf{x}$	Vector
x	Scalar

Subscripts

a	Label
a	Numbered

Research output

Oral presentations

- Femtosecond laser pulse shaping using a 4f-pulse shaper, SAIP 2012 and IONS Drakensberg 2012.
- The effect of SLM dependent dispersion on spatial beam shaping, SAIP 2013.
- The effect of spatial light modulator (SLM) dependent dispersion on spatial beam shaping, SPIE Optics and Photonics 2013. [DOI: 10.1117/12.2023286]
- A novel technique to generate and temporally shape multiple pulsed laser beams using 2D-SLMs, AIOM 2013.
- Shaping coherent light, SAIP 2014
- Ptychographic reconstruction of temporal objects, SAIP 2014

Articles

- White light wavefront control with a spatial light modulator, Article published in Optics Express in 2014. [DOI: 10.1364/OE.22.013870]
- Time domain ptychography, Article submitted to Physics Review A in 2015
- Ptychographic ultrafast pulse reconstruction, Submitted to Optics Letters in 2014

1

Introduction

As stated by Bradley and New [1] *Developments in basic physics are almost always related to advances in measurement techniques*. In this work a known phase recovery technique for high frequency electromagnetic radiation, optical and shorter wavelengths, in the spatial domain is extended to the time domain for the first time and demonstrated at optical wavelengths with excellent results. The technique is further extended to the field of optical pulse characterization again with excellent results. All experiments were done on a new pulse shaping device with the required versatility for the purpose. Parts of this dissertation have been submitted for publication or have been published in [2–4].

Direct measurement of an optical electric field is not possible as no detector is fast enough, instead the resultant intensity of the radiation is recorded with the drawback that all phase information is lost. The key challenge is to reconstruct the phase of the measured wave and several solutions to this so-called phase problem have been demonstrated [5–14].

One of the most robust spatial techniques to recover the lost phase information is ptychography. Ptychography is essentially a lens-less imaging method. The concept of ptychography is related to the solution of the phase problem in crystallography as proposed by Hoppe [15]. It was first demonstrated at optical wavelengths [16], but its scientific impact is expected to be largest at X-ray wavelengths, especially after the commissioning of high brightness coherent X-ray sources. So far, X-ray ptychography has been successfully applied in reconstructing real space objects of up to three spatial dimensions and a spatial resolution down to 16 nm has been demonstrated [17]. In ptychography the real space image of an object is reconstructed iteratively from a series of far-field diffraction patterns. Each pattern is recorded after either moving the object or the coherent illumination beam in a plane perpendicular to the propagation direction of the illumination beam. The transverse shift of the illumination beam is smaller than its spatial support, so that subsequent patterns result from different, but overlapping regions of the real space object. This ensures that the phase can be extracted. Moreover, the redundant information from overlapping regions helps to improve the convergence of the iterative algorithms. The spatial resolution is limited by the positioning accuracy, the stability of the entire set-up, and by the angular range of scattered wave-vectors that can be recorded with a sufficiently high signal-to-noise ratio.

In this dissertation, as mentioned earlier, the known spatial phase and amplitude measurement technique known as ptychography is extended to the temporal domain for the first time. As in the spatial analogue, the exit field is formally described by the product of the signal in time, more aptly referred to as the temporal 'object', and the probe pulse. Time domain ptychography then yields information on the temporal 'object' on

time scales much shorter than the duration of the probe pulse, a known limitation of standard pump probe measurement schemes. Working in this modality requires operation in one-dimensional space, namely time/frequency. In general, the one-dimensional phase retrieval problem is ambiguous and different solutions may result in the same far-field intensity measurement. In the framework of ptychography, however, the uniqueness of the solution in one and two dimensions is warranted as long as the illumination pattern is known [18].

In order to evaluate the feasibility of time domain ptychography and the subsequent pulse characterization technique based on time domain ptychography a new pulse shaping set-up capable of shaping two or more beams independently is implemented based on the device by Hornung *et al.* [19]. The pulse shaping set-up was developed to satisfy the need to temporally shape each of two or more identical beams individually. This control allows one to do a wide variety of measurements with the advantage that one can compare measurements with theoretical calculation since the input pulse shapes can be programmed at will and thus are known. In the experiments the generated temporal pulses are multiplied, through exploitation of the properties of a non-linear material, and the resultant intensity spectrum recorded with a spectrometer. Emphasis is placed on the fact that an intensity spectrum contains no phase information and therefore the task is to recover the spectral phase.

As a first step we demonstrate that the ptychographic scheme is able to reconstruct an unknown temporal 'object' uniform in space but varying with time by recovery of the spectral phase. The temporal 'object' is illuminated with a sequence of partially overlapping, time-delayed coherent probe pulses and for each time delay a far-field diffraction pattern, i.e. wavelength resolved intensity spectrum, is recorded. With the pulse shaping set-up one beam is used to generate an arbitrary temporal 'object' and the other beam a time delayed probe pulse which is multiplied in a beta-bariumborate (BBO) crystal, through the process of sum frequency generation, to produce the output as an intensity spectrogram which is recorded with a spectrometer. The process is repeated for all time delays and the resultant output is recorded as an intensity spectrogram, containing an intensity spectrum for each time delay, and used as the input to the iterative algorithm to reconstruct the temporal 'object' by recovery of the phase information. Since the temporal 'object' is realised by a known transfer function the reconstruction can readily be compared to theoretical calculation. The resulting measurements and comparisons show excellent agreement clearly demonstrating that time domain ptychography can be used to recover the phase of temporal 'objects' if the condition that the measured spectra is the result of a product of the temporal 'object' and a known probe pulse is met.

Pulse characterization is a natural extension of time domain ptychography as the pulse itself could be viewed as the temporal 'object'. A lot of work has been done in the field of pulse characterization. Since the discovery of mode-locking and ultrashort laser pulses, characterization of these pulses has been an imminent task as no known detector was, and still is, fast enough to measure such ultrashort pulses directly. In 1967 Weber [20] showed that an autocorrelation scheme together with a nonlinear process can be employed to estimate the pulse duration, such arrangement is now classified as a second order background-free intensity autocorrelation measurement. About 20 years later, Diels *et al.* [21] introduced the second order background-free interferometric auto-correlation method with the aim to not only estimate the pulse duration but to fully characterize the electric

field of ultrashort laser pulses, e.g. its spectral amplitude and phase. In the subsequent years several further ingenious schemes have been proposed and demonstrated, such as FROG [22, 23], STRUT [24], SPIDER [25], PICASO [26], MIIPS [27], SEA TADPOLE [28], shaper assisted FROG/STRUT [29] and many variations thereof. Mostly these modalities were first demonstrated at optical wavelengths but were later transferred to other spectral regions ranging from the MIR to the X-ray regime.

In order to use time domain ptychography to do pulse characterization the additional constraint that the phase of the probe pulse is also unknown has to be resolved. The phase of the probe is unknown since the probe is generated from the pulse itself in a split beam geometry by application of a known transfer function to one arm of the system. To recover the phase of the probe, the reconstruction algorithm starts with an initial guess of a flat phase which is then updated with the recovered phase every so often. During our measurements we mimic a split beam geometry with the transfer function to generate the probe implemented in one arm. This is done by applying the same transfer function to both beams before additionally applying the transfer function specific to the generation of the probe pulse. Again an intensity spectrogram is recorded in the same manner as for normal time domain ptychography above for the chosen temporal pulse shape and the resultant probe pulse. The resultant spectrogram is fed into the time domain ptychography pulse reconstruction algorithm. The reconstructions of time domain ptychographic pulse reconstruction is compared to a well known pulse characterization technique namely second harmonic generation frequency resolved optical gating (SHG-FROG) as the optical set-up for these are very similar. The versatility of our pulse shaper allowed us to use it to do SHG-FROG measurements by recording a spectrogram of an autocorrelation of the desired temporal pulse shape for analysis. Excellent agreement of recovered spectral phase was found while time domain ptychographic pulse reconstruction showed no sign ambiguity which is a known issue in SHG-FROG due to the symmetric nature of the autocorrelation used as an input to the SHG-FROG reconstruction algorithm.

The rest of this dissertation is organised as follows:

- In Chapter 2 the theoretical foundation which underlies temporal pulse shaping as well as ptychography is treated.
- In Chapter 3 an in-depth discussion of how the phase only 2D SLM can be utilised to apply complex phase and amplitude transfer functions is described.
- In Chapter 4 the double beam independent temporal pulse shaper used in all the subsequent experiments is treated.
- In Chapter 5 the proof of principle experiment showing that time domain ptychography is possible is treated.
- In Chapter 6 we show how time domain ptychography can be extended to do pulse characterization.
- in Chapter 7 we conclude and discuss future work.

2

Theory

In this chapter we look at the relevant theory behind the experimental work done which lays the foundation for the methods used to shape light both in space and time after which the theory relevant to the temporal analogue of ptychography is discussed.

Understanding of the spatial and temporal behaviour of light is necessary in order to understand how one can use optics in specific geometries in order to modify this high angular frequency (for visible light in the order of 2.7 to 4.8 rad/fs) electromagnetic radiation as no electronic devices are fast enough to do so accurately. The wavelike behaviour of light is explained and how, after some reasonable approximations are made, through Fourier optics one can calculate the spatial field after propagating through optical systems. The shaping of light is then extended to the temporal domain by explanation of how exploitation of the dispersive properties of gratings can be utilised to do so. Then the second order polarization of materials is discussed as it is critical to the measurement of our signals. Finally extending ptychography to the temporal domain is explained along with the measurement and reconstruction procedures.

2.1 Light as electromagnetic radiation

Here the treatment of light within the framework of Fourier optics is explained by starting with a general description of light as a waves of electromagnetic radiation with the coupling of the electric and magnetic fields as described by Maxwell's equations. This is followed by a description of the polarization and propagation of light through transparent media. Finally the specific case of a lens within the Fourier optical framework is underlined since it plays an important role in temporal pulse shaping.

Light behaves like a wave where both the electric **E** and the magnetic **H** fields can be expressed in the form of the time independent wave equation, known as the Helmholtz equation, as

$$\left(\nabla^2 + k^2\right)\mathbf{E} = 0 \tag{2.1.1}$$

$$\left(\nabla^2 + k^2\right)\mathbf{H} = 0 \tag{2.1.2}$$

with the wavenumber $k = 2\pi/\lambda$ if the medium of propagation is simple, i.e. linear, homogeneous and isotropic [30–32]. The transverse nature of light waves mean that the electric and magnetic fields oscillates orthogonally to the direction of their propagation. This oscillation of the electric and magnetic fields can then be decomposed into two perpendicular components which can have different phase with respect to each other. This

difference in phase between the perpendicular transverse components of the electric and magnetic field is what gives light its polarization property. Also the propagation velocity of a specific wavelength of light is dependent on the medium through which it propagates. In vacuum the propagation velocity is the speed of light c. The refractive index n is used to describe the wavelength dependent ratio of propagation velocity in a medium v_{m} to vacuum c as $n = c/v_{\mathrm{m}}$. The refractive index is a material property and as such some materials have a refractive index which is dependent on the polarization of incident light. This is mainly related to the ordering of the molecular structure in the material, i.e. the material has a uni-axial anisotropic molecular arrangement. Such a material is said to be birefringent [33]. A ray analogy is used to describe the change in direction of a wavefront crossing a refractive index boundary by Snell's law,

$$n_1 \sin\theta_1 = n_2 \sin\theta_2 \tag{2.1.3}$$

where a ray is taken as a line perpendicular to the wavefront, n_1 and n_2 is the refractive index before and after the refractive boundary respectively and θ_1 and θ_2 is the angle of the ray and a line normal to the surface where the ray is incident at the refractive index boundary. Lastly not all light incident at the refractive boundary propagates further in the medium, some is reflected at an opposite angle with the normal to the surface. Often in practice optics are coated to minimize reflections. The amount of light that enters and that is reflected by a medium can be calculated with the Fresnel equations,

$$r_{\perp} = -\frac{n_{\mathrm{i}}\cos\theta_{\mathrm{i}} - n_{\mathrm{t}}\cos\theta_{\mathrm{t}}}{n_{\mathrm{i}}\cos\theta_{\mathrm{i}} + n_{\mathrm{t}}\cos\theta_{\mathrm{t}}} \tag{2.1.4}$$

$$r_{\parallel} = +\frac{n_{\mathrm{t}}\cos\theta_{\mathrm{i}} - n_{\mathrm{i}}\cos\theta_{\mathrm{t}}}{n_{\mathrm{i}}\cos\theta_{\mathrm{t}} + n_{\mathrm{t}}\cos\theta_{\mathrm{i}}} \tag{2.1.5}$$

$$t_{\perp} = +\frac{2n_{\mathrm{i}}\cos\theta_{\mathrm{i}}}{n_{\mathrm{i}}\cos\theta_{\mathrm{i}} + n_{\mathrm{t}}\cos\theta_{\mathrm{t}}} \tag{2.1.6}$$

$$t_{\parallel} = +\frac{2n_{\mathrm{i}}\cos\theta_{\mathrm{i}}}{n_{\mathrm{i}}\cos\theta_{\mathrm{t}} + n_{\mathrm{t}}\cos\theta_{\mathrm{i}}} \tag{2.1.7}$$

where n again is the refractive index, r and t refers to the reflected and transmitted light respectively, the subscripts $_{\mathrm{i}}$ and $_{\mathrm{t}}$ refers the the incident and transmitted light respectively, the subscripts $_{\perp}$ and $_{\parallel}$ refers to the perpendicular and parallel components of the electric field respectively and θ the ray angles with respect to the surface normal. It can be seen that if layers are added in order to minimize the difference between θ_{i} and θ_{t} the reflected light will be minimized. This in combination with constructive and destructive interference from the different layers is in principle how anti-reflection coatings work. For more details see Hecht [33].

The theory thus far allows one to break a known wavefront into infinitesimal pieces and propagate each piece through vacuum and transparent materials with curved surfaces taking the coupling of the **E** and the **H** fields into account which is a rather involved and complicated calculation. Fortunately work done by Silver [34] shows that under certain conditions one can view the **E** field as a scalar component thereby ignoring the coupling imposed by Maxwell's equations. The conditions under which this simplification is valid, referred to as the *scalar conditions*, are as follows: (1) the diffracting aperture is large with respect to the wavelength of the incident light and (2) the diffracted fields are not observed close to the aperture.

The body of Fourier optics arises by making a number of assumptions to solve the complicated integrations that one encounters while solving a geometry with the propagation theory of light under the scalar conditions, most prominent of which is the small angle approximation. Here only relevant results from the theory are mentioned. The reader is referred to Goodman [30] for a thorough treatment of the subject.

In the Fourier optics regime the Fourier transform can be applied to find accurate solutions applicable to a wide variety of optical problems hence the name Fourier optics. Two approaches exist in this regime to solving problems with a standard input output geometry illustrated in Fig. 2.1 (a) for no obstruction and (b) when an obstruction is present. The

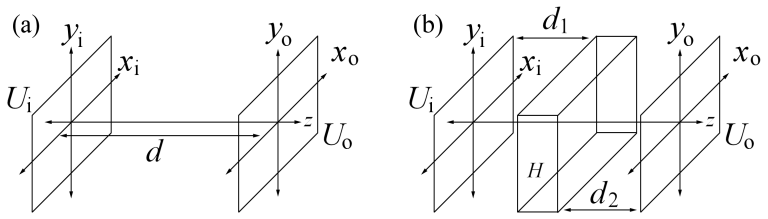

Figure 2.1: (a) Optical geometry without an optical element and (b) with an optical element.

two approaches are the Huygens-Fresnel principle and the angular spectrum method. The Huygens-Fresnel principle arose from the description of wavefront propagation by Huygens in 1678 by stating that the next wavefront would consist of the sum of wavelets with like radius each originating at equidistant points on the previous wavefront, Fresnel then amended this theory by applying the wave nature of light allowing for interference. Using the Huygens-Fresnel principle entails integrating the input field for each point on the output field while adapting the phase and intensity according to the distance between the current point and all points at the input plane. The angular spectrum method arises from linear time invariant theory and entail using the Fourier transform to calculate the angular spectrum of an input field which is then multiplied with the relevant transfer functions in order to account for the effects of propagation and optical elements after which the result is inverse Fourier transformed to find the field at the desired output plane. In the derived theory, when the optical system includes lenses, the assumption is made that the field propagates at small angles which allows for a number of approximations to be valid, further simplifying the expressions used in Fourier optical theory. Although this seems like a very limiting condition when lenses are concerned, as the angles can easily be larger than strictly required by the small angle approximation, one has to realise that the small angle can be considered with respect to the natural wavefront shape of the lens which greatly relaxes the condition for light originating at the focal plane of said lens.

An interesting effect occurs in optical systems in the far field i.e. for very big z ($z > 2D^2/\lambda$ where D is the aperture width) the output field is a spatially scaled Fourier transform of the input field. This is also true when working with lenses where the input and output fields are spaced a focal distance from the lens in a so called 2f-geometry. In this case we observe at the output field a Fourier transform of the input field scaled by the focal distance of the lens. This is important in the context of this thesis as we extensively

make use of this property of lenses in our optical design. The relation of the input and output fields in such a geometry is given by the optical Fourier transform

$$U_o(x_o, y_o) = \frac{A}{i\lambda f} \iint U_i(x_i, y_i) e^{-i\frac{2\pi}{\lambda f}(x_i x_o + y_i y_o)} dx_i dy_i \tag{2.1.8}$$

where f is the focal length of a lens used in a simple geometry such as illustrated in Fig. 2.1 (b) with the optical element replaced by a lens and the input and the output planes being spaced one focal distance from said lens.

Though not explicitly stated, the electric field consists of perpendicular polarization components which can be decomposed into a chosen perpendicular axis system. The electric field at the output of a system must be calculated along both polarization axes for the entire input field. In the system we implemented, the two perpendicular polarization components were in phase resulting in linear polarization simplifying calculation to only this axis.

The treatment thus far is mainly concerned with the spatial propagation properties of light and in the context of a Gaussian laser beam can be easily used to calculate the spatial propagation of light.

The temporal evolution of light can be considered separately, using standard Fourier theory as it applies to electric signals, where spatial overlap of the spectral components exist in the framework, as above, of isotropic, linear, homogeneous materials. Of course this implies that in order to calculate the temporal evolution of the electric field at some point, the spatial propagation calculations have to be applied to all spectral components, the sum of which is then used to calculate the resultant electric field in time at this position. The procedure has to be repeated for all positions. This sounds very involved but in practice an effort is made to ensure collinear propagation of spectral components as far as possible and when not possible using optics to ensure a volume of spatial overlap of the spectral components where the temporal behaviour of the light can be easily calculated without the need to take spatial calculations into consideration.

2.2 The grating as a spectral dispersion element

Temporal pulse shaping requires one to somehow gain access to the spectral content which make up ultrashort optical pulses. Here we explain how gratings exploit wavelength dependent diffraction by making use of a periodic surface structure, the result being that each spectral component will be diffracted at different angles by the grating. The same can be achieved using prisms but here the focus is specifically on gratings as these are the elements applied in the experimental work done.

A more concise method to find the diffraction angles of different wavelengths of light incident on a grating is described next. Gratings are optical elements with very fine periodic structures, often of the same order of magnitude as the applied wavelength of light, therefore the coupling of the **E** and **H** fields are of consequence. Due to the functional application of a grating, which is to disperse light with the main interest being the resultant direction of the dispersed spectral components, the treatment can be simplified to primarily determine the direction of constructive interference of the spectral components. The coupling of the **E** and **H** fields affects only the amplitude depending on the geometry

of the grating and can be measured if needed or calculated using finite element methods, only in special cases can analytical solutions be found.

Let us consider a grating as a spectrally dispersive optical element. As mentioned, a grating is a device with a periodic structure with a ruling spacing in the order of or larger than optical wavelengths. The periodic structure results in diffraction. The angles of the diffraction orders can be determined by deriving a relation for constructive interference for any diffraction order $m\lambda$ of the incident light,

$$m\lambda = d(\sin\alpha \pm \sin\beta) \tag{2.2.1}$$

from a simple geometry as illustrated in Fig. 2.2 by considering the total path length difference between equidistant points taken on consecutive rulings on the grating structure. It can be seen that a grating will disperse the spectral components giving each component

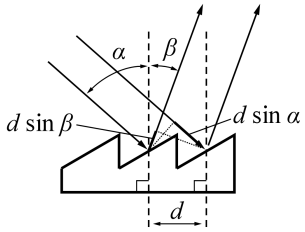

Figure 2.2: Grating geometry showing the difference in path length for light originating at equidistant points.

a unique propagation angle.

Again, if the dimensions of a grating are large in comparison to the wavelength such that the the scalar conditions are met and the angular relation between the incident and exit fields are small then standard Fourier optics theory could accurately be used to determine the properties of the grating. This is often the case when programmable wavefront shaping devices such as 2D spatial light modulators are used to implement gratings. In Chapter 3 a detailed analysis of a blazed grating when implemented on a 2D-SLM is treated to show how one can utilise the blazed grating in order to modify the amplitude of light diffracted into the ± 1 order.

The wavelength dependent angular dispersion as described by Eq. 2.2.1 translates to adding a linear spatial phase to the spectral components of light after incidence on a grating. If one considers the one dimensional case of a spectral component with wavelength λ as part of a beam $B(x,\lambda)$ incident on a grating then one can write a spatial expression for the spectral content with newly acquired propagation angles $\beta(\lambda)$ which can be translated to a spatial phase gradient $\tan(\beta(\lambda))$ after incidence on the grating as

$$B_\lambda(x) = B(x,\lambda)e^{i\tan(\beta(\lambda))x}. \tag{2.2.2}$$

From Eq. 2.2.2 one can see that the spectral content will propagate in different directions allowing access to the spectrum if allowed to propagate a distance large enough such that the spectral components spatially separate. Of course modification of the spectral components in such a way would be impractical as the dimensions of such an optical set-up is of impractical scale. In Section 2.3 we show how this property is properly utilised to access the spectral content of an optical pulse in combination with lenses.

2.3 Temporal pulse shaping

In this work temporal pulse shaping is a critical ingredient as all experiments done depends on the ability to take the pulses delivered by the laser source and shape them in the temporal domain for the specific purposes required by these experiments.

Ultra-short laser pulses are shaped using optical methods since electronic systems are not fast enough to operate in the picosecond and femtosecond regimes as mentioned in the introduction. As a result passive optical systems were developed, as early as 1973 [35], which utilise the dispersive properties of optical elements such as gratings or prisms to gain access to the spectral content of optical pulses. Since then many applications have been successfully developed using static masks at first [36, 37] later replaced by programmable devices such as the early spatial light modulators (SLM) [38, 39] leading up to modern day applications [40–42]. These spatial light modulators are capable of modifying the phase and in some cases also the amplitude of the incident light, treated in more detail in section 2.4. Here we focus on SLM based temporal pulse shaping, for a detailed review of temporal pulse shaping devices and methods refer to Weiner [40, 41].

The modern day SLM is used in conjunction with a 4f-geometry which is an imaging geometry with two lenses in a back-to-back 2f-geometry as illustrated in Fig. 2.3. The 4f-geometry results in one-to-one imaging meaning the output is an exact, or as close to as is possible, replica of the input. The first lens (L1), which is in a 2f-geometry with the input

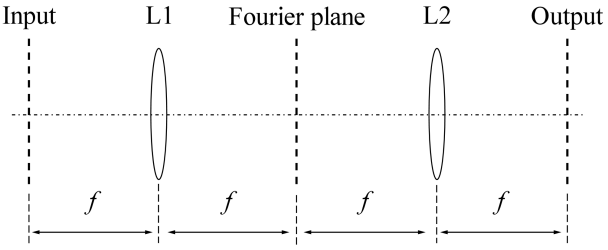

Figure 2.3: One to one imaging with a 4f-geometry showing two back to back 2f-geometries about (L1) and (L2) with the Fourier plane in the middle.

to the system and the Fourier plane, make up the first half of the symmetric 4f-geometry and its function is to perform an optical Fourier transform on the light at the input of the system according to Eq. 2.1.8 such that the angular spectrum of the light at the input plane is imaged at the Fourier plane. The second lens (L2) which is again in a 2f-geometry performs another optical Fourier transform this time on the electric field in the Fourier plane with the result that the electric field at the output has a spatial phase with reversed sign to what one would expect from an inverse Fourier transform. In practice this means the output can be considered as an inverse Fourier transform of the electric field in the spectral plane which is simply flipped 180° about the optical axis.

Access to the spectral content of the input laser pulse is gained by utilising the spectral dispersion from a grating. If a grating is placed in a 2f-geometry with a lens it can be shown using Fourier optics, when considering only one dimension, that for a spectral component represented by the simple case of a Gaussian beam profile $B_\lambda(x)$ with width σ propagating away from the grating at a wavelength dependent angle β_λ which can be

translated to a spatial phase gradient $\tan(\beta_\lambda)$ described by

$$B_\lambda(x) = \exp\left(\frac{-x^2}{2\sigma^2}\right) e^{i \tan\beta_\lambda x}, \tag{2.3.1}$$

that this spectral component will undergo an optical Fourier transform by the lens according to Eq. 2.1.8 which will result in a field at the Fourier plane $U_\lambda(X)$ given by

$$U_\lambda(X) = \frac{A}{i\lambda f}\sigma\sqrt{2\pi}\exp\left(\frac{-\sigma^2\gamma^2[X-\tan\beta_\lambda]^2}{2}\right) \tag{2.3.2}$$

with $\gamma = 2\pi/\lambda f$. From the result in Eq. 2.3.2, with reference to Fig. 2.3, it can be seen that each spectral component propagating at a different angle will be focussed to a different position at the Fourier plane of the first 2f-geometry about (L1). It should also be noted that the size of the output beam is inversely proportional to the size of the input beam while proportional to the wavelength and the focal length of the lens, as is expected from a lens. Thus the spatial optical Fourier transform properties of a lens are utilised in conjunction with a grating in order to gain access to the spectral content which makes up the temporal pulse.

The addition of a grating at the input and output of a 4f-geometry results in what is known as a 4f-shaper since this optical set-up allows for the modification of the spectral content of the laser pulse at the Fourier plane which in the specific case of the 4f-shaper is referred to as the spectral plane, illustrated in Fig. 2.4. The optical axis of the 4f-shaper is aligned with the center of the chosen dispersive diffraction order from the grating and all other orders are ignored. The relationship between the wavelength and the resultant angles of spectral components due to the grating are described in Section 2.2 and determined by Eq. 2.2.1. The resultant spectral components in the spectral plane of the 4f-shaper is, in the case of a spherical lens a collection of small points or in the case of a cylindrical lens a collection of thin lines. The density of the spectral components which makes up an optical pulse is generally very high such that the spot size of the lens is too big to resolve the individual spectral components. Instead the spectrum is seen as smeared out in the spectral plane. The spectral resolving power of the system is determined by the closest resolvable spectral components as determined by the overlap of their focal spots at the spectral plane after a Fourier optical transform, by the lens, of the product of the illumination beam with the grating itself. In a pulse shaper the spectral resolution determines the temporal window within which temporal pulse shaping can be done (calculated for our set-up in Appendix A.1). Light from the spectral plane is inverse Fourier transformed at the output plane by the second lens and a flipped output grating which results in collinear recombination of the spectral content, if the spatial effects of the transfer function applied in the spectral plane is ignored.

The description of the operation of the 4f-shaper thus far assumed that application of spectral transfer functions in the spectral plane does not alter the propagation direction of the light. In practice the spatial propagation direction of the light incident on some position at the spectral plane is modified according the gradient of the phase applied at the spectral position. This is known as spatio-temporal coupling. In Fig. 2.5 a simple example of an applied linear phase gradient is illustrated. Theory to predict spatio-temporal coupling exists [43] and methods that allow for compensation along the entire length of the beam path exist with moderate degrees of success [44, 45]. In all cases where a small

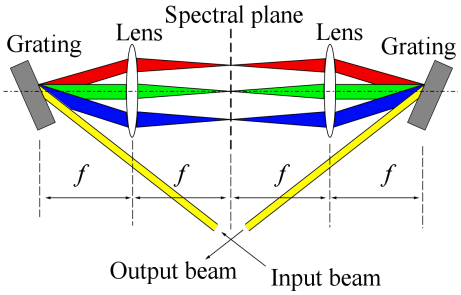

Figure 2.4: The 4f-shaper showing the placement of the gratings which disperses the spectral content indicated by three example components and how they are focussed at the spectral plane.

volume of the sample is to be examined, it is good enough to only have spatial overlap of the spectral components at a single position, an interaction volume, in the beam. This overlap region is achieved by a lens in a 2f-geometry which collects the parallel light from the grating at the output of the 4f-shaper and focuses it through a common spot such that all the spectral components overlap spatially in the focus of the lens. Thus a

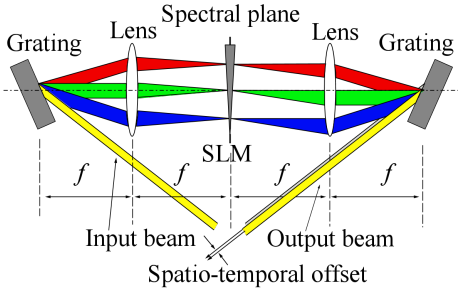

Figure 2.5: A 4f-shaper with a glass wedge at the spectral plane, which mimics a linear phase gradient, to demonstrate spatio-temporal coupling.

method to temporally shape light despite spatio-temporal coupling is given if only valid in a interaction volume at the focus of a lens in a 2f-geometry after the 4f-shaper [46].

Standard Fourier relations which applies to the temporal evolution of an electric field can be used to describe the resultant modification to temporal pulses when complex valued spectral transfer functions are applied in the spectral plane of a 4f-shaper, namely the Fourier transform and the inverse Fourier transform given by

$$f(t) = \frac{1}{2\pi}\int_{-\infty}^{\infty} F(\omega)\mathrm{e}^{\mathrm{i}\omega t}d\omega \tag{2.3.3}$$

$$F(\omega) = \int_{-\infty}^{\infty} f(t)\mathrm{e}^{-\mathrm{i}\omega t}dt. \tag{2.3.4}$$

These relations give great versatility in modification of the temporal pulses with well known relationships between the spectral and temporal plane which one can utilise to temporally shape pulses. Application of a transfer function to a pulse implies multiplication of the spectrum of the pulse with the spectral transfer function and is realised in

practice simply by illumination of a device or phase mask with the spectrum of the pulse by inserting the device or phase mask in a 4f-shaper. Programmable devices which can modify the phase and amplitude of the incident spectral components exist. These devices are discussed in the next section.

2.4 The spatial light modulator

A device capable of modifying the phase and amplitude of incident light is required in order to apply spectral transfer functions by placement of the device in the spectral plane of a 4f-shaper. The spatial light modulator (SLM) is such a device. Here we give a description of the operation of these devices.

The functioning of a SLM is based on the utilisation of nematic liquid crystals. These nematic liquid crystals are birefringent consisting of grain like particles as illustrated in Fig. 2.6 (a). When a voltage is applied across the contact layer the crystals will try to align themselves to the electric field as illustrated in Fig. 2.6 (b), according to the strength of the applied electric field along an axis referred to as the extraordinary axis. The refractive index along the extraordinary axis seen by the light with polarization along this axis is modified according to the degree of tilt of the grain like particles. In this way the optical path length of light propagating along the extraordinary axis of the nematic liquid crystal pixel cell can be adjusted by changing the voltage across the pixel. The phase difference along the extraordinary axis resulting from the application of a voltage across the contacts can be measured and a typical response curve of voltage versus phase shift is shown in Fig. 2.6 (c). A SLM consists of a 1D or a 2D array of individually controllable nematic liquid crystal pixels depending on the device. The discrete phase control of the incident light allows one to apply discreet wave-front functions. It is clear from the above

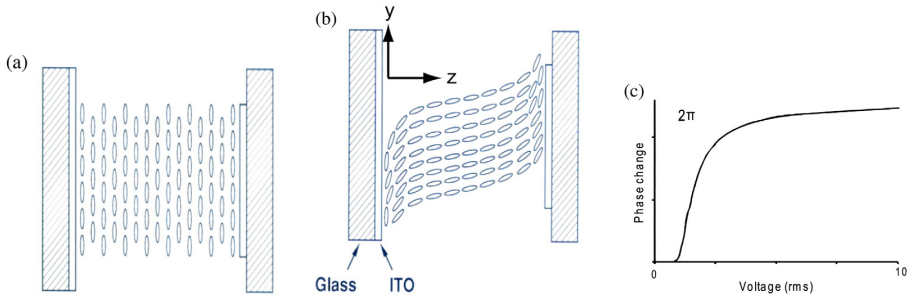

Figure 2.6: Illustration of a section view of a LC crystal. In (a) the no voltage is applied to the surface contacts, in (b) the effect of applying a voltage to the contacts is shown and in (c) a typical phase versus voltage curve is shown. (Image from Weiner [41])

description that SLMs can only modify the phase of the incident light. Amplitude shaping of the incident light is realised in different ways by 1D and 2D models of SLMs. In the 1D SLM, two back to back 1D arrays of nematic liquid crystals are used to modify the incoming light which has linear polarization at 45° with respect to the extraordinary axis of the nematic liquid crystal cells. Each of the back to back arrays are therefore capable of varying the degree of elliptical polarization which in combination with a polariser to select a specific polarisation at the output enables amplitude modification of the incident

light. In this work we used only 2D SLMs and as such the reader is referred to Weiner [40, 41] for an in depth discussion of the operation of a 1D SLM. Amplitude shaping with a 2D phase only SLM, within the context of the 4f-shaper where each vertical line of the 2D SLM acts as a one dimensional SLM for the incident spectral component, is done through the implementation of blazed gratings and is discussed in detail in Chapter 3.

The theory discussed thus far allows for the temporal shaping of laser pulses by combination of a 4f-shaper with a SLM. A critical requirement of ptychography and many pulse characterization methodologies is the ability to multiply temporal pulses. In the next section we will describe how non-linear optical materials allow us to do just that.

2.5 Non linear materials

The response of atoms and molecules to electromagnetic fields is approximately linear for small electric fields. However, when the electric field becomes very large the response becomes non-linear. This is a very useful property as these materials can be used in a specific geometry to multiply electromagnetic signals in time as will be explained below. It is exactly this property which is exploited in order to analyse the electric field by measurement of the resultant spectrum to be analysed by any of a number of phase recovery techniques. Here the focus is specifically on the mechanism by which the multiplication of two electric signals comes about.

The non-linear material response is what makes the multiplication of optical electromagnetic signals possible. A simplified description of the polarisation response of a material is given by,

$$\mathbf{P} = \varepsilon_0 \left(\chi^{(1)} \mathbf{E} + \chi^{(2)} \mathbf{E}^2 + ... \right), \tag{2.5.1}$$

where $\chi^{(1)}$ and $\chi^{(2)}$ is a first and second rank tensor etc. and the resultant polarization is a matrix. The multiplication of the signals comes about as a result of the material polarization response and as such the input polarization of the electric field plays a role. In all examples below the input polarization of the electric field is linear and the same in the cases where two are electric fields are used, thus for the purpose of highlighting how signal multiplication comes about we write the electric fields as scalar components noting that through the tensor product the resultant polarization of the output would be perpendicular to the input polarization.

Second harmonic generation (SHG), sum frequency generation (SFG) and difference frequency generation (DFG) arise due to the second order polarization response $\chi^{(2)}$ of the material being non-zero. Only materials that lack inversion symmetry can exhibit second order non-linear effects. For the rest of the discussion we only consider the linear and second order polarization.

SHG occurs when the electric field is multiplied by itself as a result of the polarization response of the material as given by Eq. 2.5.1 and this usually occurs when the the incident electric fields are collinear. In the case of SHG, the electric field is described by $E = A\cos(\omega t - \mathbf{k} \cdot \mathbf{z})$ with the $\mathbf{k}$ in the direction of $\mathbf{z}$ such that we can view the dot product $\mathbf{k} \cdot \mathbf{z} = k \cdot z$ which when substituted into Eq. 2.5.1 gives

$$\mathbf{P} = \varepsilon_0 \left[\chi^{(1)} A \cos \omega t + \frac{1}{2} \chi^{(2)} A^2 [1 + \cos(2\omega t - 2k \cdot z)] + ... \right] \tag{2.5.2}$$

from which the second order electric field generated with perpendicular polarization to the input field can be written as

$$E_{\text{SHG}} = A^2 \cos(2\omega t - k_2 \cdot z) \tag{2.5.3}$$

where $2k = k_2 = n_2 2\omega/c$ with n_2 the refractive index seen by the frequency 2ω. It is clear that the argument of the first order polarization and the second order polarization will only be in phase if the refractive index seen by ω and 2ω are the same which is not ordinarily the case as refractive index varies with wavelength. If the refractive indices mismatch and as a result the second order electric field and the second order polarization become π radians out of step they will interfere destructively. The length over which the generated second order wave becomes π radians out of step is called the coherence length and is given by

$$L_{\text{coh}} = \frac{\lambda}{4|n_2 - n_1|} \tag{2.5.4}$$

where λ is wavelength, n_1 is the refractive index seen by the frequency ω and n_2 the refractive index seen by the frequency doubled second harmonic 2ω.

In the case of SFG two electric fields, each with its own frequency ω_1 and ω_2, are considered which usually propagates non-collinearly with propagation vectors $\mathbf{k_1}$ and $\mathbf{k_2}$ given by

$$E = A_1 \cos(\omega_1 t - \mathbf{k_1} \cdot \mathbf{r}) + A_2 \cos(\omega_2 t - \mathbf{k_2} \cdot \mathbf{r}). \tag{2.5.5}$$

The second order polarization response which results in SFG for the electric field given by Eq. 2.5.5, when substituted into Eq. 2.5.1, is

$$\mathbf{P} = \varepsilon_0 \left[... + \chi^{(2)} A_1 A_2 \cos[(\omega_1 + \omega_2)t - (\mathbf{k_1} + \mathbf{k_2}) \cdot \mathbf{r}] + ... \right] \tag{2.5.6}$$

from which one can define a freely propagating electric field, again with polarization perpendicular to the input polarization, with frequency $\omega_3 = \omega_1 + \omega_2$ and propagation vector $\mathbf{k_3} = \mathbf{k_1} + \mathbf{k_2}$ given by

$$E_{\text{SFG}} = A_1 A_2 \cos(\omega_3 t - \mathbf{k_3} \cdot \mathbf{r}). \tag{2.5.7}$$

In order for the electric field to remain in phase with the polarization the refractive indices must satisfy

$$n_1\omega_1 + n_2\omega_2 = n_3\omega_3 \tag{2.5.8}$$

along the new propagation direction as given by $\mathbf{k_3}$.

In the case of DFG a similar situation arises which leads to Eq. 2.5.6 but instead the waves entering the system are ω_2 and ω_3 in which case the polarization component giving rise to DFG is described by

$$\mathbf{P} = \varepsilon_0 \left[... + \chi^{(2)} A_3 A_2 \cos[(\omega_3 - \omega_2)t - (\mathbf{k_3} - \mathbf{k_2}) \cdot \mathbf{r}] + ... \right]. \tag{2.5.9}$$

from which again one can define a freely propagating electric field, again with polarization perpendicular to the input polarization, with frequency $\omega_1 = \omega_3 - \omega_2$ and propagation vector $\mathbf{k_1} = \mathbf{k_3} - \mathbf{k_2}$ given by

$$E_{\text{DFG}} = A_3 A_2 \cos(\omega_1 t - \mathbf{k_1} \cdot \mathbf{r}). \tag{2.5.10}$$

Again in order for the generated freely propagating electric field to remain in phase with the polarization the refractive indices must satisfy

$$n_1\omega_1 = n_3\omega_3 - n_2\omega_2 \tag{2.5.11}$$

along the new propagation direction as given by $\mathbf{k_1}$. If the thickness of the non-linear material is thin enough and the incident angles small enough quasi-phase matching is achieved which greatly relaxes the phase matching conditions due to material dispersion.

In all these cases a birefringent material which lacks inversion symmetry is required to meet the phase matching condition. Even with the correct material of course the coherence length is limited by the total bandwidth of the incident electric field and the angles of the incident light. For a more extensive treatment of non-linear optics the reader is referred to New [47] and to Demtröder [48].

In the context of this work SFG is utilized extensively. We see that if the phase matching conditions are met by using the right material such as a beta-bariumborate (BBO) crystal, one can effectively multiply optical pulses as shown, which comes about due to the $\chi^{(2)}\mathbf{E}^2$ component in the material polarization as shown in the simple two spectral component example in Eq 2.5.7. In our case the phase matching conditions are more relaxed as we use a thin crystal and illuminate it at shallow angles resulting in so quasi-phase matching whith adequate performance for our purposes. The phase matching conditions and the intensity response of the non-linear material limits us to a small interaction volume. Fortunately the same solution which is implemented to solve the problem of spatio temporal coupling, Section 2.3, meets these additional constraints namely the placement of a lens in a 2f-geometry after the 4f-shaper.

With the ability to multiply signals in time, coupled with the ability to temporally shape optical pulses, we are able to demonstrate time domain ptychography which will be discussed in the next section.

2.6 Time domain ptychography

Time domain ptychography is a natural extension of ptychography. Ptychography as mentioned is a lens-less imaging technique which can be used to determine both amplitude and phase of an illuminated object. As such ptychography requires the recording of a far field diffraction pattern, $I_n(X,Y)$, of some object, $o(x,y)$, illuminated by a known probe beam at a known position $p(x-x_1, y-y_1)$, as described by the relation,

$$I_n(X,Y) = \left|\mathscr{F}\left\{o(x,y)p(x-x_1,y-y_1)\right\}\right|^2 \tag{2.6.1}$$

where the operator $\mathscr{F}$ refers to the Fourier transform. The object is illuminated at several positions by translating either the object or the illumination source in a plane perpendicular to the beam and in each case a far field diffraction pattern is recorded. It has to be noted that the strength of this modality is that the size of the illuminating beam is much larger than the smallest recoverable feature of the object. The phase information is lost in the intensity measurements of the far field diffraction patterns but can be recovered by using said diffraction measurements as an input to the ptychographic iterative engine (PIE) [49].

One can find an analogy to ptychography when working with a pulsed laser source in the temporal domain (Time domain ptychography). The beam position is similar to a

temporally delayed probe, $P(t-\Delta t)$, and the far field diffraction pattern is equivalent to a recorded spectrum, $I_n(\omega)$, resulting from the product of a temporal probe at the time delay with a temporal object, $O(t)$, as expressed by

$$I_n(\omega) \quad = \quad \left|\mathscr{F}\left\{O(t)P(t-\Delta t)\right\}\right|^2. \tag{2.6.2}$$

Multiplication of the time delayed probe pulses with the temporal object is often referred to as probing the temporal object. A data set recorded by probing the temporal object at different time delays t_n each time recording the phase less intensity spectrum as a collection of intensity spectra $S(\omega, t_n)$, referred to as an intensity spectrogram, can then be fed into the ptychographic reconstruction algorithm modified for application in one dimensional operation space, which we refer to as the time domain ptychographic reconstruction engine (TD-PIE). It is only important that the temporal position of the probe is known and for the probe pulse to overlap in time to some extent with the probe pulse of another measurement for every intensity spectrum recorded in order to use the TD-PIE. The requirement of temporal overlap of the probe pulses determines the size of the time step needed between measurements. The resolution of the reconstructed measurement is determined by the spectral window instead of the step size between measurements and the temporal window is determined by the spectral resolution as determined by the Fourier relationship between time and frequency. Typically the recordings are equidistant in time spaced Δt apart such that $t_{n+1} = t_n + \Delta t$ to cover a temporal range starting at $t_1 = t_{\text{start}}$ and ending at $t_N = t_{\text{start}} + N\Delta t$ as is the case for experiments done in this work. The collection of the data is illustrated in Fig. 2.7 as obtained in a cross-correlation fashion. A temporal object indicated by the solid line (this can be a programmed temporal

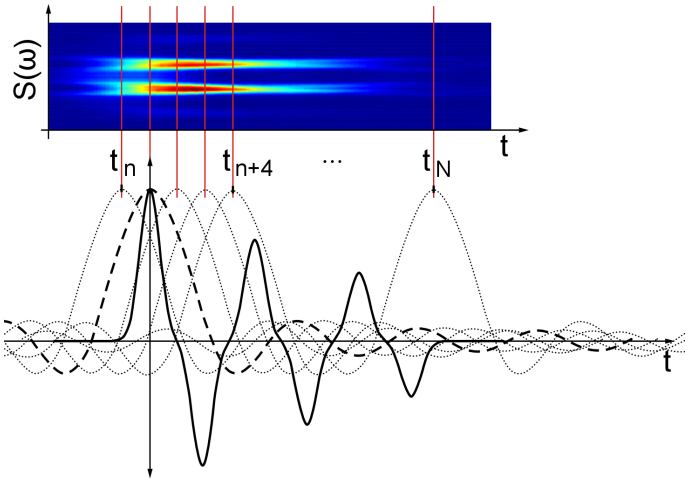

Figure 2.7: Illustration graphically depicting the measurement of an intensity spectrogram, inlay at the top, by multiplication of a probe at different time delays indicated by the dashed lines with a temporal object indicated by the solid line as an example of a time domain ptychography measurement.

object function as in our case or a material response function which is activated by some mechanism) is multiplied by the probe pulse, indicated by the dotted lines, at different

temporal delays and the intensity spectrum of the resultant multiplication is recorded for each time delay in a what is referred to as an intensity spectrogram shown at the top.

As with ptychography, where the illuminating beam can be much larger than the smallest resolvable feature of the object, so too it will be shown in the temporal analogue, that the probe pulse can be much longer than the smallest resolvable temporal feature of the temporal object. In contrast with classic pump probe measurement techniques where the resolution is limited by the probe pulse duration, in time domain ptychography the resolution is limited by the bandwidth of the spectrometer. In practice this limit will be determined by the range of the spectrum where there is sufficient signal to noise ratio.

The reconstruction algorithm works as follows. Once an intensity spectrogram is recorded by multiplication of a temporal object at different time delays with the temporal probe pulse, the recorded intensity spectrogram is fed into the TD-PIE illustrated in Fig. 2.8. The algorithm starts by estimating an arbitrary choice of object function. An exit

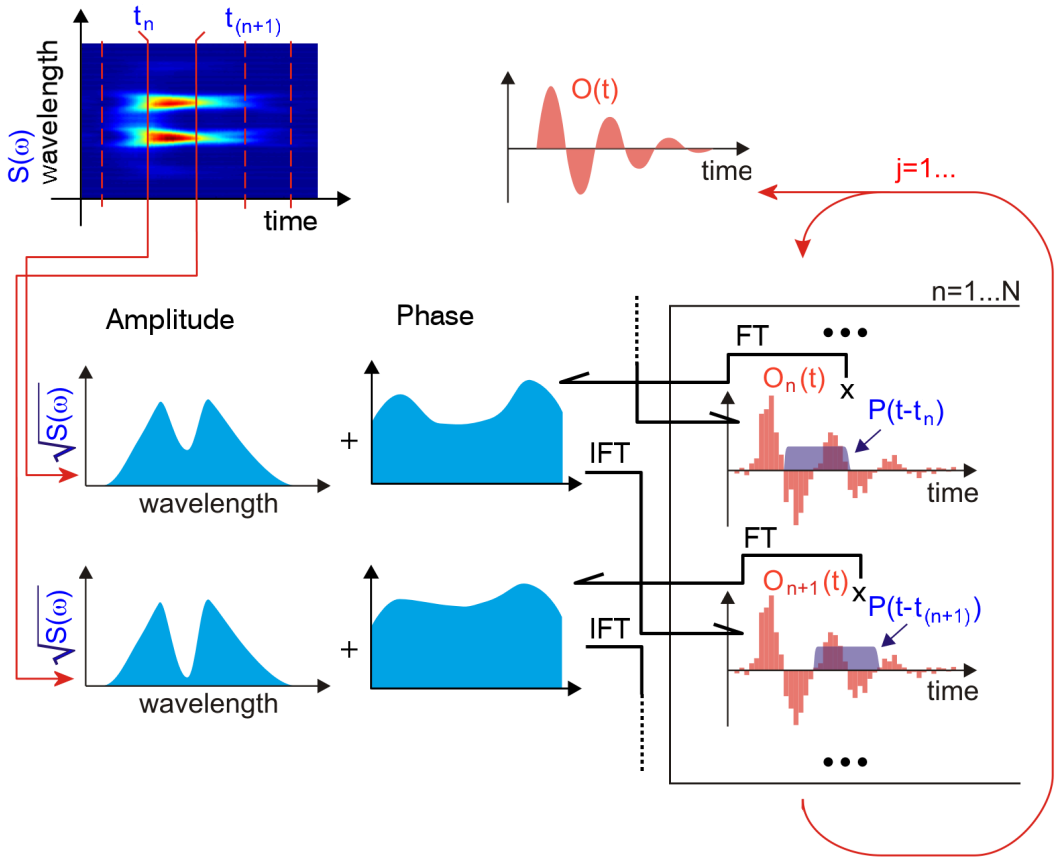

Figure 2.8: Illustration of the functioning of the reconstruction algorithm. The measured intensity spectrogram, inlay at the top left, is used to update the guess of the spectrum for each time delay t_n sequentially repeated j times to produce the reconstructed temporal pulse inlay at the top right.

field is then calculated by taking the product of the object function $O_n(t)$ and the known probe function at a specific time delay $P(t - t_n)$,

$$G(t, t_n) = O_n(t)\ P(t - t_n). \tag{2.6.3}$$

An updated exit field is then calculated in the spectral domain $G'(\omega, t_n)$ by taking the square root of the measured spectral amplitude $I_n(\omega, t_n)$ and the spectral phase of the exit field

$$G'(\omega, t_n) = \sqrt{I_n(\omega, t_n)} \exp\left(\angle \mathscr{F}\left\{G(t, t_n)\right\}\right) \tag{2.6.4}$$

and inverse Fourier transformed back to the time domain to find the updated exit field in time $G'(t, t_n)$. The difference between the current exit field and the updated exit field is then used to correct the object function

$$\begin{aligned} O_{n+1}(t) &= O_n(t) + \beta\, U(t - t_n) \\ &\quad \times [G'_n(t, t_n) - G_n(t, t_n)] \end{aligned} \tag{2.6.5}$$

with the weight or window function

$$U(t) = \frac{|P(t)|}{\max(|P(t)|)} \frac{P^*(t)}{|P(t)|^2 + \alpha} \tag{2.6.6}$$

where the constants α and β are bounded by $\alpha < 1$ and $\beta \in]0 \ldots 1]$. This is done sequentially for each of the whole numbered $n = 1..N$ time delays of the probe pulse after which the procedure can be repeated using the calculated object function $O(t)$ as the starting seed for the next loop j.

In order to prove time domain ptychography, a temporal object as well as a probe pulse is required. Ideally we want to have control over both the temporal object and the probe pulse such that we are able to evaluate the efficacy of the proposed modality. We implemented a multi-beam temporal pulse shaper, described in Chapter 4, capable of generating two identical laser pulse beams and temporally shaping them to realise different temporal objects and probe pulses. In the next chapter we will look in detail how a 2D SLM can be used to apply complex valued spectral transfer functions.

3

Pulse shaping with a phase only 2D SLM

Current 2D SLMs are only capable of phase modulation, however pulse shaping by modification of spectral amplitude and phase is possible using a 2D-SLM in a 4f-shaper configuration by utilizing blazed gratings [42]. Also, such a set-up could be easily extended to shape multiple beams [19] treated in the next chapter. Most recently we have shown [4] in the spatial domain that when a 2D SLM is used to implement a phase and basic amplitude mask the phase behaviour in the $\pm$ 1 diffraction orders is ideal irrespective of wavelength. Here we explain how a 2D SLM can be used to realise phase and amplitude transfer functions, underlining the detail of the effect of combination of phase and amplitude shaping and the required phase compensation that results.

3.1 Transfer functions with a 2D SLM

In order to apply a complex valued transfer function on a 2D-SLM placed in the spectral plane of a 4f-shaper one needs to be able to modify both the amplitude and phase of the spectral components incident on the device. Conceptually phase modification can be easily understood as the 2D-SLM has the ability to directly modify the phase of the incident light, modification of the amplitude however is not so obvious. Here we show that both amplitude and phase modulation of the spectrum of light can be achieved with a phase only 2D SLM by utilizing the properties of gratings, more specifically blazed gratings [19, 42]. First a conceptual explanation is given of how a sequence of blazed gratings can be used to apply a spectral transfer function after which a more rigorous mathematical treatment follows.

To conceptually understand how blazed gratings are used to realise a spectral transfer function a simplified example is given where a 2D-SLM is placed in the spectral plane of a 4f-shaper and the incident light source has only three spectral components, red, green and blue illustrated in Fig. 3.1. Each spectral component is focussed by a cylindrical lens as part of the 4f-shaper only in the horizontal plane resulting in an elliptical spectral slice which is incident on a vertical section of the 2D-SLM encoded with a blazed grating. The position of spectral components vary along the horizontal axis and are determined by the spectral dispersion angle due to the grating at input of the 4f-shaper, thus the horizontal axis is indicated by ω. To each spectral component the blazed grating where it is incident looks as if it is infinitely wide as shown in the section view on a-a. The diffraction from said grating will propagate mainly in the +1 diffraction order depending on the efficiency of the blazed grating. If the rest of the optical set-up is aligned along the direction of this diffraction order such that all other diffraction orders can be ignored,

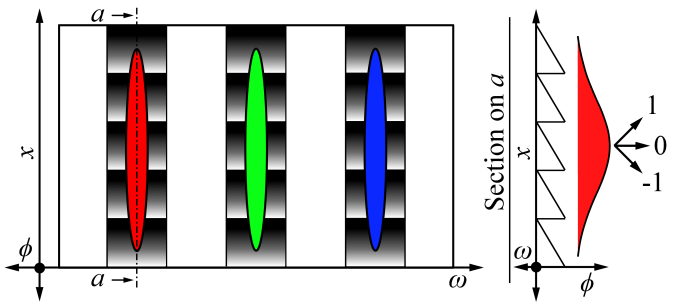

Figure 3.1: Application of blazed gratings in the vertical direction to modify spectral content. Three example wavelengths represented by different colours are shown on exaggerated blazed gratings to illustrate the principle of utilizing blazed gratings.

then one can see how amplitude modulation can be achieved by altering the amplitude of the programmed blazed grating, hence its efficiency, as illustrated in Fig. 3.2 (a). As such an amplitude of zero would mean all light is reflected into the zero order and a phase amplitude of 2π for the specific spectral component means, in the ideal case, all light propagates in the direction of the +1 diffraction order. Phase modification is illustrated conceptually in Fig. 3.2 (b) where two consecutive spectral components which fall on two separate blazed gratings represented by the brown and the green lines show the constant phase difference between them $\Delta\phi$ as a result of a translation of one of these two gratings with respect to the other.

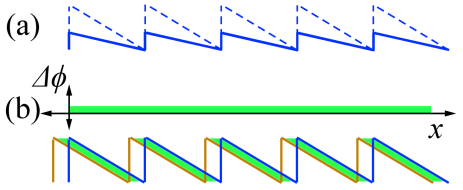

Figure 3.2: Blazed grating used to do (a) amplitude modulation, by decreasing the amplitude of the blaze grating, and (b) phase modulation, by introducing a lateral shift relative to another blazed grating. The resultant modification is observed in the ± 1 diffraction orders.

Now let us look at a more mathematically rigorous treatment. We have shown, in the spatial regime, that the application of blazed gratings on a 2D-SLM to selectively divert light from areas on the 2D-SLM where specific phase functions are applied into the ± 1 diffraction orders results in ideal phase behaviour for a broadband source [4] despite collinear illumination of the 2D-SLM. Here we extrapolate on the expression we derived Spangenberg *et al.* [4] for blazed gratings in order to apply the result to a 2D-SLM used in a 4f-shaper configuration. If the applied periodicity of the blazed grating is much larger than the wavelength of the incident light and the angles are small we can use standard Fourier optic theory to treat the blazed phase grating illustrated in Fig. 3.3. A mathematical expression can be written for an infinitely extending blazed grating as the windowed selection of a linear phase convolved with a comb as,

$$g(x) = \left[e^{i\frac{\theta}{p}x}\text{rect}\left(\frac{2}{p}x\right)\right] \circledast \sum_{n=-\infty}^{\infty} \delta(x - x_0 - np)$$

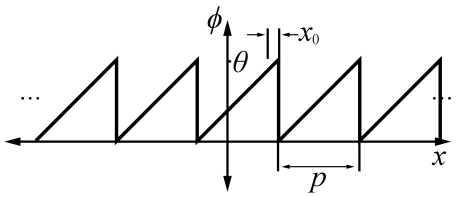

Figure 3.3: Cross-section of a linear phase gradient with pitch p wrapped around a phase maximum of θ translated relative to the zero position by x_0

where from Fig. 3.3, the position of the blazed grating x_0 is defined relative to zero, the amplitude of the blazed grating implemented as a phase function is given by θ, the pitch of the grating is given by p and n is an integer representing the duplicated blazed sections. This expression can be simplified using standard Fourier relations by taking the Fourier transform of Eq. 3.1.1 and simplifying,

$$\begin{aligned} G(X) &= 2\pi\left[\delta\left(X-\frac{\theta}{p}\right) \circledast \operatorname{sinc}\left(\frac{p}{2}X\right)\right] \times \sum_{n=-\infty}^{\infty} \delta\left(X-\frac{2\pi n}{p}\right) \times \mathrm{e}^{-\mathrm{i}Xx_0} \\ &= 2\pi \operatorname{sinc}\left(\frac{p}{2}\left[X-\frac{\theta}{p}\right]\right) \times \sum_{n=-\infty}^{\infty} \delta\left(X-\frac{2\pi n}{p}\right) \mathrm{e}^{-\mathrm{i}Xx_0} \\ &= 2\pi \sum_{n=-\infty}^{\infty} \operatorname{sinc}\left(\frac{p}{2}\left[\frac{2\pi n}{p}-\frac{\theta}{p}\right]\right) \delta\left(X-\frac{2\pi n}{p}\right) \mathrm{e}^{-\mathrm{i}\frac{2\pi n}{p}x_0} \\ &= 2\pi \sum_{n=-\infty}^{\infty} \operatorname{sinc}\left(\pi\left[n-\frac{\theta}{2\pi}\right]\right) \delta\left(X-\frac{2\pi n}{p}\right) \mathrm{e}^{-\mathrm{i}2\pi n\frac{x_0}{p}} \end{aligned} \tag{3.1.1}$$

where X is the co-ordinate in transformed space and x is the co-ordinate in normal space, and then taking the inverse Fourier transform to find

$$g(x) = \sum_{n=-\infty}^{\infty} \operatorname{sinc}\left(\pi\left[n-\frac{\theta}{2\pi}\right]\right) \mathrm{e}^{\mathrm{i}\frac{2\pi n}{p}x} \mathrm{e}^{-\mathrm{i}2\pi n\frac{x_0}{p}}, \tag{3.1.2}$$

which is an elegant expression of a blazed grating as a sum of weighted infinitely extending linear phase functions where the parameter n now represent diffraction orders.

The expression derived in Eq. 3.1.2 is clearly separable into key components namely amplitude, phase and propagation direction which makes it very easy to calculate masks to represent transfer functions. Only the ± 1 diffraction orders of the masks are generally utilized in practice therefore let us consider the case where $n = \pm 1$. The amplitude scaling factor which is only dependent on the blaze grating phase amplitude θ is given by

$$S(\theta) = \operatorname{sinc}\left(\pi\left[\pm 1-\frac{\theta}{2\pi}\right]\right), \tag{3.1.3}$$

the relative phase shift dependent on the ratio of the relative starting position x_0 and the pitch p of the blazed grating is given by

$$\Delta\phi(x_0) = \mathrm{e}^{\mp\mathrm{i}2\pi\frac{x_0}{p}} \tag{3.1.4}$$

and the directional wave front with the angle inversely proportional to the pitch p is given by

$$D(p) = \mathrm{e}^{\pm\mathrm{i}\frac{2\pi}{p}x}. \tag{3.1.5}$$

The derived equation does not consider the total optical path length change. This comes about due to the decreased phase height of the blazed grating. If one considers this decrease in phase height as a physical decrease in the phase height of the blazed grating then the light must travel an extra distance outside of the grating through air with a lower refractive index causing a decrease in optical path length which in turn results in a decrease in phase. In practice the physical length stays the same but the index of refraction changes which results in the same effect.

Compensation for this effect can be easily done by adding a constant amount of phase equal to the area of phase lost due to the decreased phase amplitude. This compensation results in shifting the blaze up such that it pivots about the centre point of the full blaze as illustrated in Fig. 3.4. To prove this consider: if we assume the difference in phase to

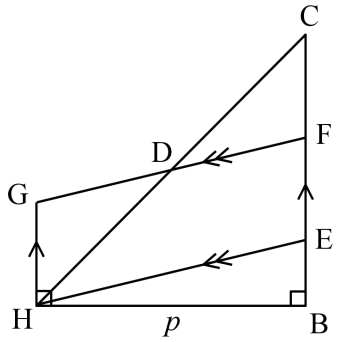

Figure 3.4: Illustration of an enlarged view of a single blazed ruling with additional lines to aid in the derivation of the required phase adjustment when the amplitude of the blazed grating is adjusted.

be directly related to the difference in area which results from decreasing the amplitude of the blazed grating then we can easily use the geometry in Fig. 3.4, which shows an enlarged illustration of a single blazed grating ruling as the triangle AREA_{CBH}, to derive an expression to correct for the introduced phase error. Given a triangle AREA_{HBC} and an arbitrary point is chosen between B and C called E to construct triangle AREA_{HBE} ,which represents the required modified blazed grating section with the required blaze amplitude indicated by BE, then one can describe the difference in area by triangle AREA_{HEC} which represents the phase error introduced due to the decrease of the amplitude of the blazed grating. In order to compensate for this lost phase one must add it by shifting line HE parallel vertically upwards creating a new line GF which forms a parallelogram $\text{AREA}_{\text{HEFG}}$. The area of parallelogram $\text{AREA}_{\text{HEFG}}$ must be equal to the triangle AREA_{HEC} which represents the phase error for which one wants to compensate. If the intersection at point D between line HC and line GF is chosen such that it is in the middle of line HC, which intuitively makes sense as one can see that the phase lost in AREA_{DCF} would be gained in AREA_{DHG}, then the lines GD and DF would also be equal in length because point D is a cross point on two lines bounded by parallel lines. Thus the triangles AREA_{DCF} and AREA_{DHG} are equivalent because the sides DH = DC, DG = DF and $\angle_{\text{GDH}} = \angle_{\text{FDC}}$ and one can state that the parallelogram $\text{AREA}_{\text{HEFG}} = \text{AREA}_{\text{HEC}}$. Defining the required phase amplitude BE in terms of the maximum phase amplitude BC as BE $= \theta A$ where BC $= \theta$

with $0 \leq A \leq 1$ then one can write

$$\begin{aligned} \text{AREA}_{\text{HEFG}} &= \text{AREA}_{\text{HEC}} \\ &= \frac{1}{2}p(\text{BC} - \text{BE}) \\ &= \frac{1}{2}p\theta(1-A) \end{aligned} \tag{3.1.6}$$

which gives the phase error. Normalising the calculated phase error in Eq. 3.1.6 to the pitch of the grating one can write an expression for the phase error per unit pitch ϕ_{err} as

$$\phi_{\text{err}} = \frac{1}{2}\theta(1-A). \tag{3.1.7}$$

The result is very useful since it implies that the phase compensation due to modification of the amplitude can be easily done as it is relative to the actual maximum amplitude used in implementing the blazed grating, as such its functioning is not sensitive to perfect calibration. If the device is optimised for efficiency in the first order then the amplitude of the blazed grating is $\theta = 2\pi$ and Eq. 3.1.7 can be written in the more recognizable form [50] as,

$$\phi_{\text{err}} = \pi(1-A). \tag{3.1.8}$$

Here we have shown how phase and amplitude shaping can be done using a phase only 2D-SLM. In the next chapter we will describe a multi-beam temporal shaper where the 2D-SLM is utilised to apply spectral transfer functions using blazed gratings as described in this chapter to apply amplitude and phase modulation to the spectrum of the input pulses.

4

Multi-beam temporal pulse shaper

We designed a scalable multi-beam shaper where a SLM at the input of a 4f-shaper is loaded with a phase mask which diffracts the incoming beam thereby generating multiple beams. The implemented set-up is unique in that it does not require the light to be focussed on the diffracting phase mask which opens up the potential to also do spatial shaping of the beam however this was not done in this work. The experimental set-up was configured to enable the use of two beams, each of which can be individually shaped in time in order to have full control over the experimental parameters for ease of comparison to theoretical calculation. We refer to this set-up as the double beam temporal shaper (DUBTESP)[1]. The experimental measurements required in order to examine the various phase recovery modalities require cross-correlation of the generated pulses. For this purpose the second order non-linear response of a beta-bariumborate (BBO) crystal is utilised to multiply the two pulses with each other through the process of sum frequency generation (SFG). The resultant intensity spectrum can then be recorded with a spectrometer.

4.1 Optical set-up

The experimental set-up illustrated in Fig. 4.1 uses a binary holographic grating loaded on the 2D SLM (S1) to generate two divergent beams, each beam goes through the 4f-shaper and is incident on a separate area on a 2D SLM (S2). On each area on (S2) the required transfer function is encoded as explained in Chapter 3 using a sequence of blazed gratings. The periodicity of the chosen gratings on (S2) matches the periodicity of the holographic grating on (S1). This matched SLM grating pair is encoded with blaze angles chosen on each respective shaper area such that the output energy is optimized for the parallel propagating +1 and -1 diffraction orders after incidence on (S2). The output of the system, as determined by the applied transfer functions to generate the probe $P(t)$ and the object $O(t)$ pulse, is focused by a lens in a 2f-geometry with respect to the output of the shaper and the BBO crystal, into the BBO crystal which is positioned in the volume of spatial overlap of the spectral components such that spatio-temporal coupling can be ignored. The resultant output after multiplication of the two signals in the BBO crystal through the process of sum frequency generation is collected by a spectrometer which records the intensity spectrum.

[1]The spelling is chosen to be difficult to pronounce in the spirit of all things difficult to pronounce such as ptychography, pterodactyl, pituitary etc. Another argument could be 'Large hadron collider', 'All your base are belong to us' and 'This is gentleman'.

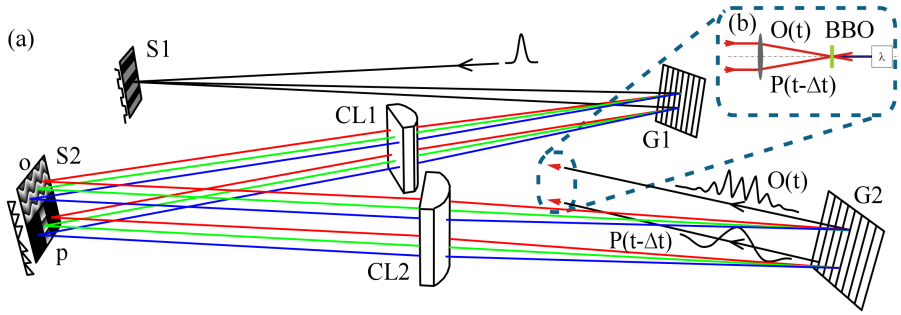

Figure 4.1: (a) Schematic of the experimental set-up showing how the first 2D-SLM (S1) is used to generate two beams each of which is individually temporally shaped on the second 2D-SLM (S2) to generate two output pulses, a temporal object $O(t)$ and a probe pulse $P(t)$. (b) Inlay of the optical set-up where the multiplication of the temporal object and the probe in a BBO crystal by sum frequency generation is recorded by a spectrometer.

The pulse source is a 80 Mhz Ti:sapphire oscillator generating pulses of approximately 80 to 110 fs duration. Both SLMs are Holoeye 1920x1080 devices with a pixel pitch of 8 µm and active area 15.36 mm wide by 8.64 mm high calibrated to have a linear phase response from zero to 2π at 800 nm. The cylindrical lenses both have focal lengths of 130 mm and the blazed gratings (G1) and (G2) are ruled with 600 lines/mm. The SLM gratings are encoded with a periodicity of 160 µm.

The cylindrical lenses in the 4f-shaper were chosen to have a spot size in the order of the pixel pitch for an input beam with an approximate beam diameter of 2 mm. From Fourier relations we know that the temporal response of the set-up will be a multiplication of the spectral focal width and the pixel pitch each considering its specific shape. We calculated the temporal envelope due to the spectral width of the focus of the cylindrical lens in the spectral plane to be a Gaussian with a FWHM of 6760 fs, see Appendix A.1.

The matched SLM gratings on (S1) and (S2) introduce quadratic phase in the same way a grating pulse stretcher/compressor [51, 52] does. The quadratic phase introduced can be readily calculated and compensated for in the programmable spectral transfer functions. The dispersion angles due to the grating can be used to calculate the optical path lengths for the respective spectral components after which a fit can be done to the data to extract the temporal delay and quadratic chirp, see Appendix A.2. The resultant calculations show that when using a grating pitch of 160 µm and propagation distance between the gratings of 45 cm the pulse accumulates an additional negligible 8 fs^2 quadratic spectral phase.

In order to use the described double beam temporal shaper, calibration and characterization of the set-up is required which will be discussed in detail in the next section.

4.2 Calibration

The double beam temporal shaper (DUBTESP) we built has two main components integral to its functioning: the phase response of the SLMs and the characteristics of the 4f-shaper. The phase response of both SLMs needs to be calibrated for optimal operation after which the 4f-shaper has to be characterized by determining the position of the spectral components in the spectral plane as well as measuring the amplitude response of the

applied blazed gratings in the spectral plane for both beams. Once this calibration and characterization is complete the shaper can be used to optimise the pulses from the pulse source such that experiments can be done from an optimal starting point.

4.2.1 Calibration of the SLM

The Holoeye SLM device is operated like an extra display connected to a computer. A known calibration procedure [53][2] is followed which allows one to calibrate the device such that intensity settings sent from the computer, in the range $]0..1]$, linearly maps to an introduced phase shift of the incident light on a pixel in the range of $]0..2\pi]$ for the calibrated wavelength.

Since the source is broadband the calibration will not be correct for all wavelengths, conveniently though, transfer functions are implemented by the use of blazed gratings working in the +1 and -1 diffraction orders thus phase adjustment for all spectral components will behave ideally, therefore correctly, as explained in Chapter 3 Eq. 3.1.2. The mismatch of the phase calibration at wavelengths other than the calibration wavelength results in a modification to the amplitude of the different spectral components. In our experiments, with a full width half maximum (FWHM) bandwidth of approximately 10 nm, this effect is small enough to neglect. In the case of systems with a broader bandwidth this effect can be compensated for by measurement of the amplitude response in the first order for each spectral component when the height of the blaze is adjusted on the SLM in the spectral plane.

4.2.2 Characterisation of the 4f-shaper

In order to characterise a 4f-shaper the spectral position in the spectral plane relative to the SLM has to be determined and the amplitude response of the device measured. To do these measurements we used an Avantes spectrometer, with spectral range from 200 nm to 1100 nm and a resolution of 0.25 nm, removing the crystal and focussing the light from the output of the 4f-shaper for each beam into the spectrometer consecutively.

Wavelength calibration for each beam was done by selecting fixed width slices from the spectrum at the spectral plane with the SLM (S2) by the application of a transfer function which has a transmission of zero for all wavelengths that do not fall within the range defined by the slice and one for all wavelengths that do. The position of the slice is then scanned across the face of the 2D-SLM and a spectrometer, placed in the relevant output beam of the set-up, is used to measure the resultant spectrum from which the position of the slice in wavelength is determined. The positions thus determined is then mapped to the pixel coordinate which is known from the programmed slice on (S2). The spectrum only illuminates about a third of the face of the 2D SLM (S2), as such there are positions where we cannot map the spectral position to pixel position from measurement. A second order polynomial is fitted to the measured mapping of pixel position versus wavelength in order to extrapolate the mapping to positions on (S2) where the intensity was too low to reliably record a measurement. The resultant fit on the measured mapping data is stored as a look-up table for each beam which is used by the program which generates the masks to implement transfer functions.

[2] Dudley [53] in Appendix A.1

To determine the amplitude response in the respective +1 and -1 diffraction orders for each beam incident on one half of the 2D-SLM (S2), the intensity in said diffraction order is measured and recorded by application of identical blazed gratings across the entire face of the 2D-SLM (S2) and varying the height of the programmed blazed gratings from zero to one in 256 steps. Again we can assume that the variation with wavelength of the amplitude response is small enough to neglect for our pulses with approximately 10 nm bandwidth. This simplifies calibration as the attenuation of the individual spectral components can be ignored meaning the resultant intensity spectrogram can be integrated for each step during the recording of the amplitude lookup table resulting in a single function applicable to all wavelengths. The amplitude to blaze angle lookup table for each beam is again stored in a file for use by the program which generates the masks to implement transfer functions.

4.2.3 Calibration verification and optimization

Once the device is calibrated and characterized we can verify its correct operation in terms of temporal and morphological modification of the input pulse by cross-correlation measurements of selected transfer functions applied to the beams. A cross-correlation measurement x_{xc} requires the multiplication of a pulse x_1 with another pulse x_2 for all time delays τ given by

$$x_{\mathrm{xc}}(t) = \int_{-\infty}^{\infty} x_1(t) \cdot x_2(t-\tau)dt. \tag{4.2.1}$$

The cross-correlation is realised by application of the appropriate spectral transfer functions. We generate an arbitrary choice of signal x_1 by multiplication of the pulse spectrum $P(\Omega)$ by the required transfer function $H(\Omega)$,

$$x_1(t) = \mathscr{F}^{-1}\left\{P(\Omega)H(\Omega)\right\}, \tag{4.2.2}$$

where Ω is calculated relative to the carrier frequency $\Omega = \omega - \omega_0$. The time delayed second function is realised by multiplication of the pulse spectrum $P(\Omega)$ by a linear phase gradient which results in a temporal shift,

$$x_2(t, \Delta t) = \mathscr{F}^{-1}\left\{P(\Omega)\mathrm{e}^{\mathrm{i}\Delta t\Omega}\right\}, \tag{4.2.3}$$

where Ω is calculated relative to the carrier frequency $\Omega = \omega - \omega_0$. The multiplication of these signals are then realised in a BBO crystal through sum frequency generation and an intensity spectrum is recorded as $|\mathscr{F}\left\{x_{\mathrm{xc}}(t)\right\}|^2$ which contains no phase information.

For these measurements the resultant output is recorded with a spectrometer covering the range of 300 nm to 545 nm with a resolution of 0.18 nm as an intensity spectrogram by taking a set of measurements for a range of time delays Δt. First we investigated an example of a phase only transfer function to verify correct operation of applied phase transfer functions. This was done using a sinusoidal phase transfer function

$$H(\Omega) = \mathrm{e}^{\mathrm{i}A\sin(\tau\Omega)} \tag{4.2.4}$$

calculated about the carrier frequency with $\Omega = \omega - \omega_0$. We used $\tau = 400$ fs and $A = 2.4$ which results in temporal replicas spaced 400 fs apart for one beam and applying

a range of temporal delays Δt, from -2000 fs to 2000 fs in steps of 10 fs, to the other beam. The measurement is illustrated in Fig 4.2 (a) where we can see excellent agreement with the expected temporal positions of the replicas as well as excellent morphological agreement between the measured cross-correlation and its theoretical counterpart. We conclude from this that the developed double beam temporal shaper accurately applies phase transfer functions. Next we applied an amplitude transfer function to verify that the phase compensation (Chapter 3 Eq. 3.1.7) is done correctly. We chose

$$H(\Omega) \quad = \quad \cos(\tau\Omega) \tag{4.2.5}$$

as our amplitude transfer function with $\tau = 500$ fs, which is a double pulse transfer function resulting in two pulses spaced 500 fs apart. We applied the double pulse transfer function to the one beam and again applied a range of time delays Δt, from -1000 fs to 1000 fs in steps of 10 fs to the second pulse. Again we see excellent agreement of the expected temporal positions of the measured double pulse and excellent morphological agreement of the measured double pulse and its theoretical counterpart.

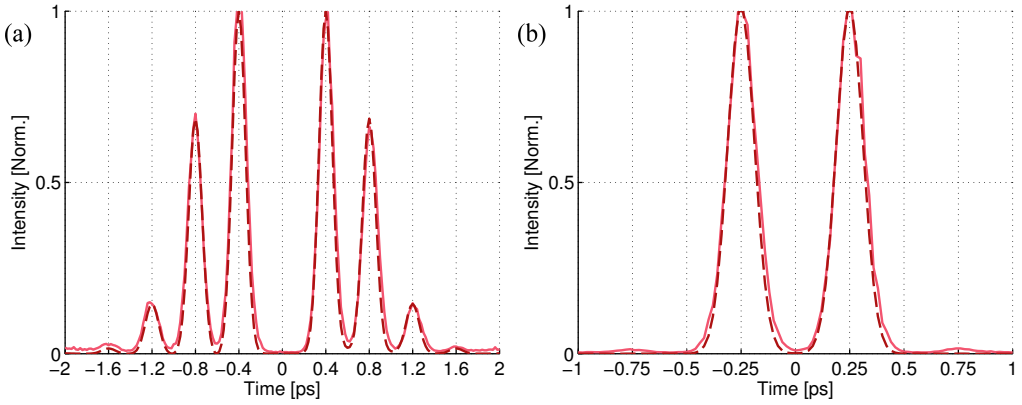

Figure 4.2: (a) Cross-correlation of a pulse with temporal pulse replicas indicating correct temporal and morphological behaviour of the shaper when a phase only spectral transfer function is applied and (b) a cross correlation of a pulse and a double pulse indicating the phase compensation is done correctly.

Having verified that our DUBTESP works we can optimise the pulses from the source. First we determine the exact time zero, which might not be the same for both pulses due to slightly different path lengths through the optical system. To do this we take a cross correlation measurement of the unaltered pulse in one beam and a time delayed pulse in the other and use the position of the measured maximum to update the relative time zero of the pulse shaper in the program. Once this is done we can use any of a number of methods to determine the spectral phase of the laser pulses and apply a compensation phase such that subsequent experiments are done from an optimal starting point with Fourier limited pulses, i.e. pulses with a flat spectral phase. Further we determine the temporal amplitude response of the system by measurement of the product of both pulses shifted in time by the same time delay Δt through application of a linear phase gradient transfer function $H_1 = H_2 = \exp(i\Delta t\Omega)$ over the temporal range of interest. This measurement is then used to correct the amplitude of intensity spectra taken at specific time delays.

We have implemented a unique double pulse temporal shaper and shown that it is capable of shaping two pulses with excellent accuracy. We can now use this device in further experiments to do a proof of principle experiment to demonstrate time domain ptychography and pulse characterization based on time domain ptychography.

5

Time domain ptychography: Proof of principle

Direct measurement of the electric field of light is not possible as no detector is fast enough to do so. The same holds for temporal pulses on the time scale of pico- and femtoseconds as mentioned in the introduction. In order to measure these ultrafast optical pulses the intensity of the spectral components that make up a temporal pulse is recorded as an intensity spectrogram. This is achieved, in brief, by separation of the spectral content onto an array detector which broadly speaking records the intensity of each, again losing the phase information. In this chapter we show for the first time that we can use our new method, time domain ptychography, to reconstruct a wide variety of temporal objects by recovery of the spectral phase.

Time domain ptychography is an extension of ptychography which is a spatial phase recovery technique as described in Chapter 2 Section 2.6. Formally the reconstruction algorithm requires as its input intensity spectra recorded after multiplication of a known probe pulse with an unknown object pulse for different time delays of the probe pulse. In order to evaluate the efficacy of the method our unique double beam temporal pulse shaper (DUBTESP) is employed, see Chapter 4, since it allows us to apply arbitrary spectral transfer functions to each of the two individual beams and record the resultant product of the resultant pulses as an intensity spectrogram. The advantage of having control over the pulse shape of both beams is that we can readily compare the reconstructions from the measured phase-less intensity spectra to their theoretical counterparts.

We intend to show that time domain ptychography shares several of the measurement advantages of its spatial counterpart. These are as follows: First, in ptychography the size of the illuminating beam can be large in comparison to the smallest resolvable spatial feature thus we expect, in the temporal analogue, that the length of the probe pulse can be much longer than the shortest resolvable temporal feature. Second, in ptychography only a few far field diffraction patterns need to be recorded by illumination of overlapping regions on the spatial object in order to reconstruct said spatial object thus we expect, in the temporal analogue, that the step size between subsequent temporal delays of the probe pulse can be large as long as there are regions of temporal overlap between them.

We start by explaining how an intensity spectrogram is measured and defining the spectral transfer functions used to generate the temporal object functions. Next we investigate how the quality of reconstruction is influenced by the time step between subsequent spectra by a root means square difference comparison of reconstructions and finally we investigate the influence of the reconstruction algorithm parameters, α and β, by again looking at how the RMS difference changes with the number of iterations. Finally we

show that we can reconstruct any arbitrary temporal object function with a range of probe pulses which vary in length.

5.1 Measurement of an intensity spectrogram

In order to record an intensity spectrogram we record the resultant intensity spectrum of the multiplication of a temporal object and a time delayed probe pulse for a series of time delays. The temporal object is generated by the application of a selected spectral transfer function to one of the beams, the object beam, in the DUBTESP. The probe pulse is generated by application of the spectral slice transfer function. First we look at the definition of the probe pulse before the transfer functions used to generate the the different temporal object functions are discussed.

A time delayed probe pulse is generated by application of a spectral slice $\Delta\Omega$ transfer function formally defined by

$$H_{\mathrm{p}}(\Omega) = \left\{ \begin{array}{ll} \mathrm{e}^{-\mathrm{i}\Omega n\Delta t} & \text{for } |\Omega| \leq \frac{\Delta\Omega}{2} \\ 0 & \text{otherwise} \end{array} \right\} \tag{5.1.1}$$

where Ω is the relative frequency defined around the carrier frequency ω_0 given by $\Omega = \omega - \omega_0$, n is the sample number and Δt is the temporal distance between subsequent probe samples. This probe pulse generated by a spectral slice we refer to as a spectral slice probe. The sample number n starts at a whole number which can be negative for negative time delays of the probe pulse and is incremented by one after every measurement until the temporal sampling range is covered for N total steps. The resultant set of intensity spectra is referred to as the measured intensity spectrogram and can be fed into the time domain ptychography reconstruction algorithm. The transfer function given by Eq. 5.1.1 results in a time delayed temporal function with a sinc envelope. The spectral slit transfer function was chosen as it can easily be applied and the duration of the resultant temporal pulses easily varied by modification of $\Delta\Omega$. Measurements of intensity spectrograms were done for a set temporal objects for each of three probe pulse lengths. The theoretical probe pulses are plotted in Fig. 5.1 for the chosen slit widths of 6 nm, 3 nm and 1.5 nm in red, green and blue respectively with temporal full width half maximum durations of the intensity of approximately 314 fs, 613 fs and 1277 fs respectively.

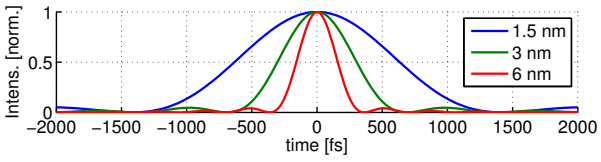

Figure 5.1: Theoretical probe pulses generated by taking spectral slices of different widths nl. 6 nm, 3 nm and 1.5 nm resulting in probe pulse lengths of approximately 314 fs, 613 fs and 1277 fs respectively .

A set of arbitrary temporal objects were generated by the application of a variety of spectral transfer functions. These are divided into three categories in the discussion below according to their properties. The categories are phase and amplitude spectral transfer functions, polynomial phase spectral transfer functions and sinusoidal phase spectral

transfer functions. In each subsequent definition the relative angular frequency Ω is defined again around a carrier frequency ω_0 as $\Omega = \omega - \omega_0$. The transfer functions used to generate the temporal objects that belongs to the set is discussed next as well as the used parameters relevant to the transfer function.

Two phase and amplitude spectral transfer functions were chosen, a pulse train with exponential decay and a double pulse. The pulse train spectral transfer function is given by

$$H_{\text{pulses}}(\Omega) = \frac{1-\mathrm{e}^{-\gamma}}{1-\mathrm{e}^{-\gamma(M+1)}} \sum_{m=0}^{M} (\pm 1)^m \mathrm{e}^{-\mathrm{i}m\Omega\tau-\gamma m} \tag{5.1.2}$$

where γ is an exponential decay constant affecting the amplitude of the resultant pulse replicas, the number of pulse replicas is given by $M+1$ and τ is the temporal spacing between the pulse replicas. A choice of $+1$ or -1 for the factor $(\pm 1)^m$ results in a pulse train where the subsequent envelope of the temporal replicas are all positive or alternating in sign respectively. The alternating pulse train with exponential decay is interesting because it resembles what one could expect to measure from a material response whereas the non-alternating pulse train is an example of an exotic pulse shape. Both versions of the transfer function were applied, as part of the measurement set, to generate temporal objects with alternating ($\pm 1 \rightarrow -1$) and non-alternating ($\pm 1 \rightarrow 1$) pulse trains each with six replicas ($M+1=6$) with exponential decay ($\gamma = 5$) spaced 400 fs apart ($\tau = 400$ fs).

The double pulse spectral transfer function, which as the name implies generates a temporal object which is a double pulse, is given by

$$H_{\text{dbl}}(\Omega) = \cos(\Omega\tau) \tag{5.1.3}$$

where τ specifies the temporal separation of the double pulse. The double pulse is a typical example of a transfer function that one could apply in a temporal shaper. It is useful, for example, to do collinear shaper assisted pulse characterization [29]. For the measurement set we generated a double pulse temporal object made up of two replicas spaced 500 fs apart by application of the double pulse transfer function with $\tau = 500$ fs.

The chosen polynomial spectral transfer functions can be generated by application of a spectral transfer function with different valued parameters where the phase contains quadratic and higher order phase terms given by,

$$H_{\text{poly}}(\Omega) = \mathrm{e}^{\mathrm{i}(a\Omega^2+b\Omega^3+c\Omega^4)}, \tag{5.1.4}$$

where an assigned value to a, b and c results in quadratic, third and fourth order spectral phase. These high order spectral phase terms are known as chirp. The most well known of these is quadratic phase, also known just as chirp, as it results in a linearly increasing instantaneous frequency in the temporal pulse. Chirp arises due to the wavelength dependence on propagation velocity of light through transparent materials and is commonly compensated for with prisms and gratings [52, 54]. Higher order chirp can also accumulate as a pulse propagates through an optical system but is considered more exotic. Temporal objects for the measurement set with higer order phase were generated by application of the spectral transfer function in Eq. 5.1.4 with $a = \pm 10^4$ fs^2 and $a = \pm 2 \times 10^4$ fs^2, $b = \pm 5 \times 10^5$ fs^3 and $c = \pm 5 \times 10^6$ fs^4 where in each case all other parameters were zero.

A sinusoidal spectral phase transfer function was chosen as a phase only transfer function which results in multiple temporal replicas of the input pulse,

$$H_{\sin}(\Omega) \quad = \quad \mathrm{e}^{\mathrm{i}A\sin(\Omega\tau+\phi)} \tag{5.1.5}$$

where A is amplitude, τ determines the spacing in time between the pulse replicas and ϕ is just a constant phase added to the argument of the sine which acts to translate the function with respect to the spectral axis. The sinusoidal phase transfer function effectively behaves like a grating resulting in temporal diffraction orders i.e. pulse replicas. How many pulse replicas are generated and their amplitudes depends on the amplitude A of the phase grating and their spacing depends as mentioned above on the parameter τ. Temporal objects for the measurement set was generated by setting $\tau = 400$ fs and $A = \pi/2$, $A = 2.4$ and $A = \pi$.

A total of 15 temporal objects were used in the measurement set as given above, recording an intensity spectrogram for each with the three different probe pulses to have a resulting measurement set of 45 intensity spectrograms. A selection of these is chosen to show the reconstruction results in the next section.

5.2 Reconstruction of an arbitrary temporal object

Reconstruction of a selection of temporal objects measured with different length probe pulses from the measurement set by using the time domain ptychographic reconstruction algorithm is shown here to illustrate that we can use time domain ptychography to reconstruct arbitrary temporal objects. The full set of reconstructions from the measurement set can be found in Appendix B. First we discuss the general trends with respect to the choice of the reconstruction parameters β, α and Δt, from Chapter 2 section 2.6, after which we illustrate these by a selected choice of examples.

5.2.1 Reconstruction parameters

The choice of the reconstruction parameters is nearly arbitrary, mainly affecting the number of iterations needed to perform a good reconstruction. The following reconstruction trends will be highlighted with respect to the parameters used in the reconstruction algorithm: there is a required degree of temporal overlap between subsequent probe pulse measurement spectra and further, within the bounds of the time step requirement, loosely a bigger value for β and/or the time step Δt and/or a smaller value for α all result in faster reconstruction of the temporal object. In order to evaluate a reconstruction we can calculate the intensity spectrogram from the reconstructed temporal object and compare it to the measured intensity spectrogram by taking the root mean square difference between them.

Each reconstruction parameter plays a specific role in the reconstruction algorithm. The temporal delay Δt between subsequent used intensity spectra from the measured intensity spectrogram determines the amount of overlap between subsequent measurements. The different reconstruction step sizes are obtained by using only every κ'th measurement, where κ is a positive non zero integer smaller than the total number of intensity spectra which makes up the intensity spectrogram used. Thus the relative time step Δt_{r} can be a multiple of the measurement time step Δt_{m} as $\Delta t_{\mathrm{r}} = \kappa \Delta t_{\mathrm{m}}$. All time

domain ptychography related measurements were made with a step size of $\Delta t_{\mathrm{m}} = 20$ fs. As mentioned time domain ptychography does not require a square relation in the time frequency sampling space, the only requirement is that subsequent recorded spectra must have a degree of overlap of the probe pulse. Since fewer spectra are used per iteration, we calculate the relative number of iterations as $N_{\mathrm{rel}} = N/\kappa$ used during reconstruction. The main role of β is as a weighting factor determining how strongly the newly calculated temporal object is applied and α determines the fall-off rate of a window centered about the current temporal position which will be affected by the application of the newly calculated temporal object.

To highlight the trends we selected a medium complexity temporal object and recorded intensity spectrograms with two different length spectral slice probe pulses, 3 nm and 6 nm, which is used as the input to the reconstruction algorithm. A double pulse temporal object was chosen which was generated by application of a co-sinusoidal spectral amplitude transfer function, Eq. 5.1.3, with $\tau = 500$ fs. In Fig. 5.2 the RMS difference between each respective measured and reconstructed intensity spectrogram is plotted against the relative number of iterations of the reconstruction algorithm for different values of the reconstruction parameters Δt, β and α.

The respective comparisons of the resultant intensity spectrogram from the 3 nm spectral slice probe pulse is shown in (a), (c) and (e), and the 6 nm spectral slice probe pulse is shown in (b), (d) and (f). In (a) and (b) we show the results when values for Δt_{r} of 20 fs, 100 fs, 200 fs, 300 fs and 400 fs are used. In (c) and (d) we show the results when values for β of 0.2, 0.4, 0.6, 0.8 and 0.95 are used. Finally in (e) and (f) we show the results when values for α of 0.01, 0.05, 0.1, 0.2, 0.3 are used. In all, with the exception of the parameter under scrutiny, we used $\Delta t_{\mathrm{r}} = 200$ fs, $\beta = 0.4$ and $\alpha = 0.1$.

In Fig. 5.2 (a) it can be seen that for any choice of Δt_{r} a good reconstruction can be found except for a time step of $\Delta t_{\mathrm{r}} = 20$ fs which is still a reasonable reconstruction, however in (b) one can see that for a large time step $\Delta t_{\mathrm{r}} = 300$ fs or 400 fs, the reconstruction fails. This is due to there not being enough overlap between the probe pulse at subsequent temporal positions. We also see that the reconstruction time decreases for a bigger time step and at the same time the quality improves a small amount.

From Fig. 5.2 (c) and (d) it is clear that for a bigger choice of β the reconstruction time decreases and also there is a small degradation of quality albeit very small.

From Fig. 5.2 (e) and (f) we see that for smaller values of α the reconstruction algorithm is quicker to find a solution however the quality of the solution is less for the case where $\alpha = 0.01$.

From Fig. 5.2 (c), (d), (e) and (f) we again see that the convergence with number of relative iterations is extremely fast for the chosen parameters.

Comparison of Fig. 5.2 (a), (c) and (e) with (b), (d) and (f) seems to indicate that for a shorter probe pulse the reconstruction is faster. This effect could be related to the length of the probe pulse but could also be related to the signal to noise ratio (SNR) as longer pulses are lower in intensity due to the narrower band bass filter and thus the resultant measured intensity spectrogram will have a lower SNR. Note the difference in SNR between the two sets is an artefact of the size of the area to which the SNR is normalised and is not indicative that that short probe pulses result in worse reconstructions. The accuracy with which the probe pulse is modelled in the reconstruction could also play a role, if the probe is represented inaccurately at the spectral edges of the selected slice then this effect will

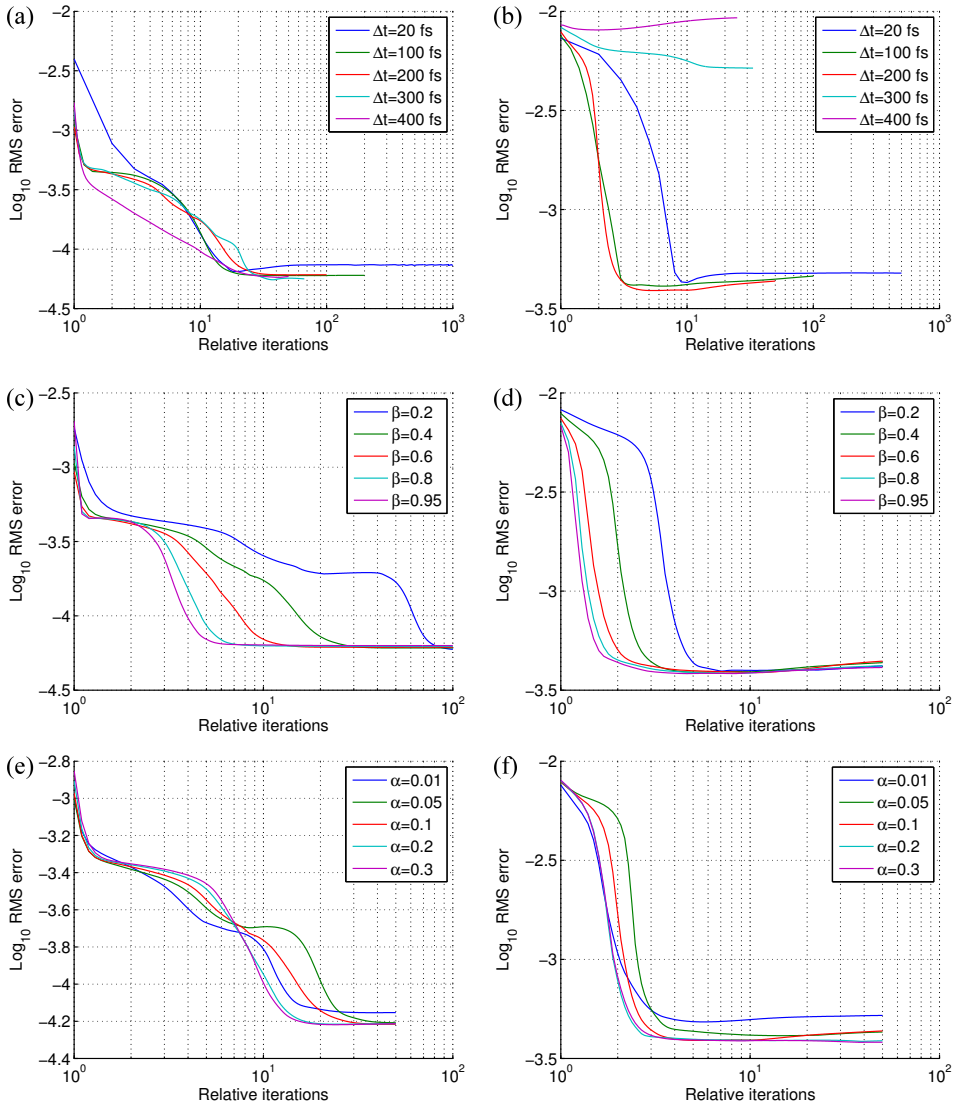

Figure 5.2: Plots of RMS errors for different values of the reconstruction parameters Δt, β and α against the relative number of iterations (c.f. text). The RMS plots of different values for the time delay used between subsequent intensity spectra Δt is shown in (a) and (b) for the intensity spectrogram recorded with spectral probe widths of 3 nm and 6 nm respectively. The RMS plots of different values used for the weighting factor β in reconstructions is shown in (c) and (d) for intensity spectrograms recorded with spectral probe widths of 3 nm and 6 nm respectively. The RMS plots of different values for α is shown in (e) and (f) for the intensity spectrogram recorded with spectral probe widths of 3 nm and 6 nm respectively.

also play a bigger and bigger role as the spectral slice becomes narrower.

In Fig. 5.3 we plot the RMS difference between the measured and reconstructed intensity spectrograms against the number of iterations for different spectral slice probes, namely (a) 1.5 nm, (b) 3 nm and (c) 6 nm, for the case when the measured intensity spectrogram is not pre-processed and when it is pre-processed. We used a sinusoidal phase spectral transfer function which generally gives a good signal to noise ratio in the measurement as an example (Eq. 5.1.5 with $A = \pi/2$ and $\tau = 400$) to underline the

effect of pre-processing of measured intensity spectrograms. The pre-processing involves subtracting a basis noise level from the entire spectrogram, filtering fast oscillations and subtracting the difference between the first spectrum and the last spectrum in the spectrogram. From Fig. 5.3 we can see that when the SNR decreases, as is the case for narrower

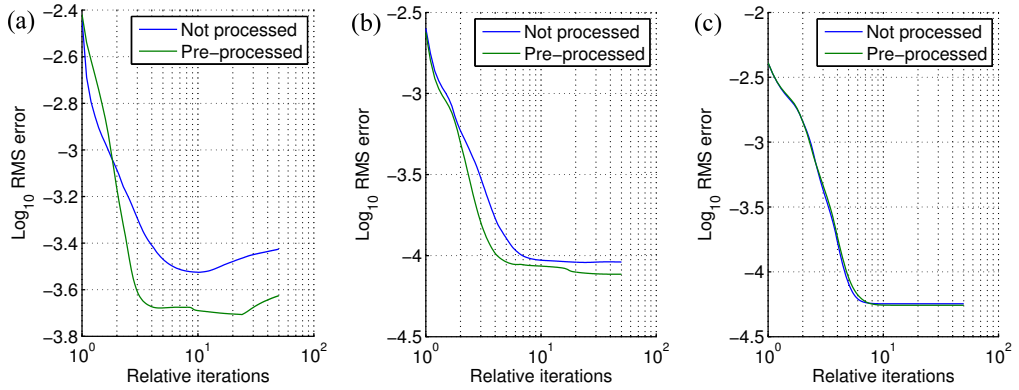

Figure 5.3: Plots of RMS versus relative iterations (c.f. text) for filtered and unfiltered for probe pulse widths of (a) 1.5 nm, (b) 3 nm and (c) 6 nm.

spectral slits, pre-processing improves reconstruction quality and speed.

The selected example illustrates that the choice of reconstruction parameters is arbitrary. As a general rule bigger time steps should be favoured albeit the time step must be small enough such that subsequent probe pulses overlap by a sizeable amount, roughly the overlap should not be smaller than 30%, larger values of β should be favoured minding the fact that a slight decrease in reconstruction quality results as β increases, α should be chosen small but not too small and if the SNR is not optimal reconstructions can be improved by pre-processing.

Based on our analysis we chose $\Delta t_{\mathrm{r}} = 200$ fs, $\beta = 0.4$ and $\alpha = 0.1$ for all reconstructions performed in the next section and Appendix B.

5.2.2 Reconstruction results

Reconstruction of the various temporal objects were calculated by using the measured intensity spectrograms as the input to the time domain ptychographic reconstruction algorithm. The resultant reconstructions are shown in Figs. 5.4, 5.5 and 5.6.

In Figs. 5.4, 5.5 and 5.6, each respective figure shows an inlay of the measured intensity spectrogram which were used as the input to the iterative reconstruction algorithm along with an inlay of a spectrogram numerically calculated from the reconstructed temporal object (the reconstruction recovers both the amplitude and phase of the electric field of the temporal object) for comparison. Further the resultant reconstructed temporal object is plotted in amplitude and phase, dashed red and blue lines respectively, along with its theoretical counterpart, solid red and blue lines, for comparison. The same temporal object functions are reconstructed in Figs. 5.4, 5.5 and 5.6 with the difference that the intensity spectrograms used as input to the reconstruction algorithm were recorded with different spectral slice probe pulses. For all sub figures in Fig. 5.4 the 6 nm spectral

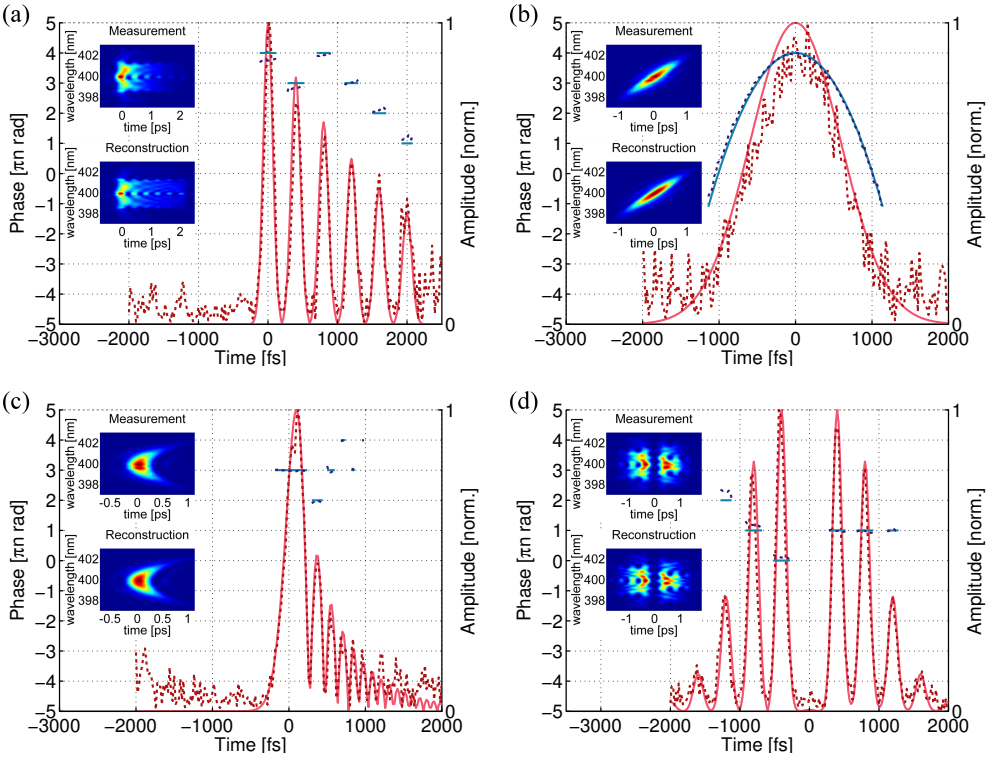

Figure 5.4: Reconstruction pulse generated by taking a 6 nm spectral slice. Alternating pulse train shown in (a). Pulse with quadratic phase of -20000 fs^2 shown in (b). Pulse with third order phase of 500000 fs^3 shown in (c). Pulse with sinusoidal phase modulation with amplitude of 2.4 shown in (d).

slice probe was used, for all sub figures in Fig. 5.5 the 3 nm spectral slice probe was used and for all sub figures in Fig. 5.5 the 1.5 nm spectral slice probe was used. The temporal objects used in Figs. 5.4, 5.5 and 5.6 are, (a) an alternating pulse train with 6 replicas decaying exponentially generated with a phase and amplitude transfer function where $M = 5$, $\gamma = 5$ and $\tau = 400$ fs, (b) a chirped pulse generated with a polynomial transfer function where $a = -20000$ fs^2, (c) a higher order chirped pulse generated with a third order polynomial transfer function where $b = 5 \times 10^5$ fs^3 and (d) temporal replicas generated with a sinusoidal spectral phase transfer function where $A = 2.4$ and $\tau = 400$ fs. All resultant reconstructions were corrected with the measured intensity response of the DUBTESP as explained in Chapter 4. The chosen reconstruction parameters were $\beta = 0.4$, $\alpha = 0.1$ and $\Delta t = 200$ fs in Figs. 5.4, 5.5 and 5.6. The input spectrograms used in Fig. 5.6 had to be pre-processed as the intensity of the measured signal was lower due to the narrow width of the slit used to generate the probe pulse which resulted in noisier measurements. In all cases the reconstruction reached a stable solution after at most 500 iterations i.e. 50 relative iterations. A complete set of reconstruction examples from our measurement set can be found in Appendix B as stated before.

Some observations that we make from the reconstructions are: The chosen probe pulse is generated as mentioned by choosing a spectral slit width which results in a decrease in energy present in the probe pulse making measurements with longer probe pulses i.e.

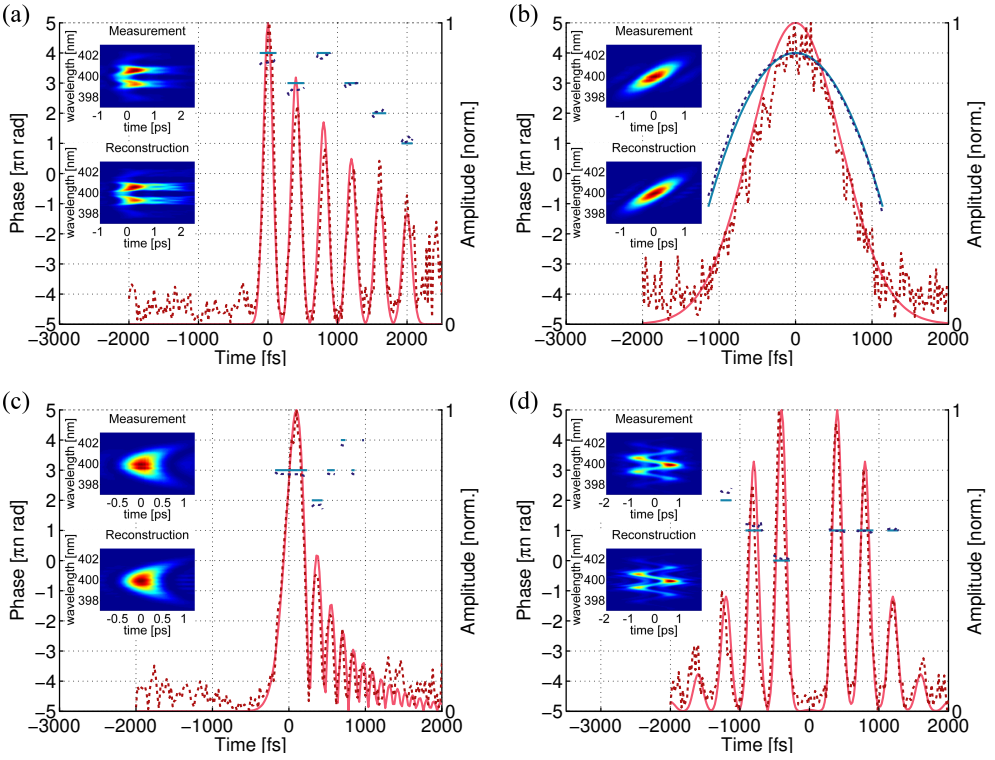

Figure 5.5: Reconstruction pulse generated by taking a 3 nm spectral slice. Alternating pulse train shown in (a). Pulse with quadratic phase of -20000 fs^2 shown in (b). Pulse with third order phase of 500000 fs^3 shown in (c). Pulse with sinusoidal phase modulation with amplitude of 2.4 shown in (d).

narrower spectral slits, noisier. This is evident by comparison of the resultant reconstructions of the four temporal object functions where the input intensity spectrograms was measured with a 6 nm, 3 nm and 1.5 nm probes in Figs. 5.4, 5.5 and 5.6 respectively. We also note that the retrieved phase of the alternating pulse train jumps with π between subsequent temporal replicas as expected.

In all cases agreement of reconstructed temporal objects with their theoretical counterpart is excellent. We see that all temporal objects probed with the three probe pulses of different length, can be reconstructed. This result is a feat in itself as it is the first time, to our knowledge, that it has been shown that a probe pulse longer in duration than the temporal features it is used to resolve was able to do so. This is especially a noteworthy result in the case of the 1.5 nm temporal probe pulse as the pulse length of such a pulse is approximately $10\times$ the duration of the shortest temporal feature resolved.

We have shown that ptychography can be extended to the time domain and that it can be used to reconstruct a wide variety of temporal object functions some with temporal features $10\times$ shorter than the probe pulse duration. We have also shown that the choice of reconstruction parameters mainly influences the number of reconstructions with the exception that when the time delay between subsequent probe pulses become too large, the reconstruction fails.

We extend time domain ptychography to pulse characterization in the next chapter.

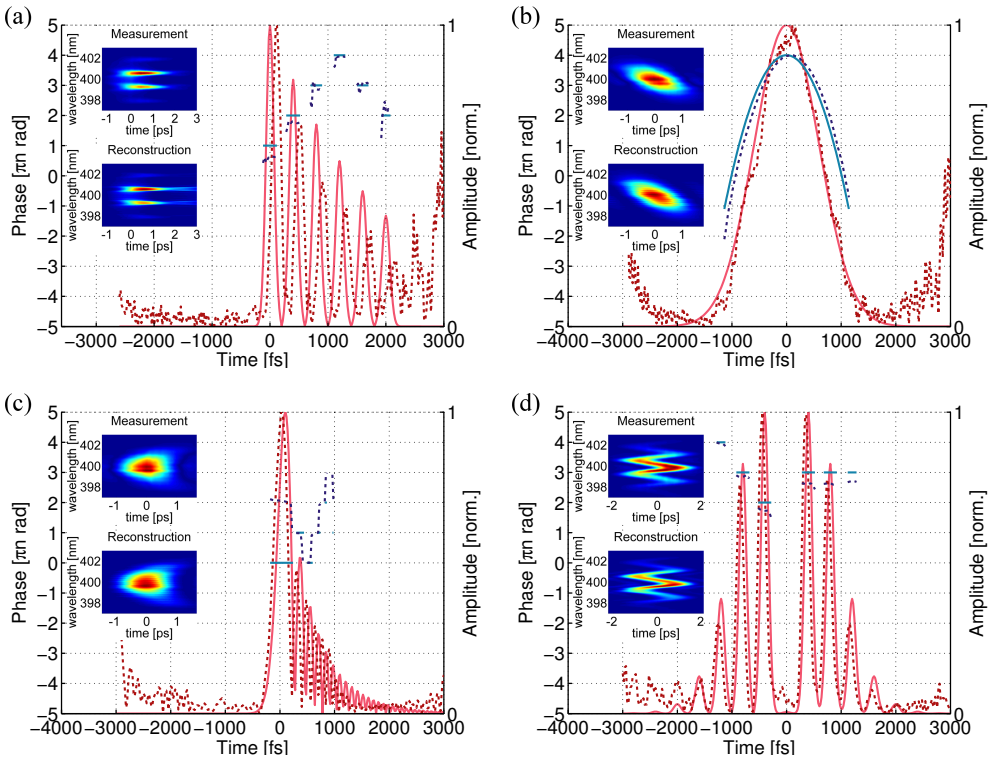

Figure 5.6: Reconstruction pulse generated by taking a 1.5 nm spectral slice. Alternating pulse train shown in (a). Pulse with quadratic phase of -20000 fs^2 shown in (b). Pulse with third order phase of 500000 fs^3 shown in (c). Pulse with sinusoidal phase modulation with amplitude of 2.4 shown in (d).

6

Time domain ptychography: Pulse characterization

Pulse characterization in most ultrafast laser systems is done without the need of a secondary source. In most if not all cases the beam itself is used to do pulse characterization eg. FROG [22, 23], STRUT [24], SPIDER [25], PICASO [26] and MIIPS [27]. In this chapter we implement an updated ptychographic iterative reconstruction algorithm in order to use time domain ptychography to characterize laser pulses using the pulses themselves.

In time domain ptychography a so called 'temporal object' is reconstructed from a measured intensity spectrogram by recording the resultant spectra of a cross-correlation of the unknown temporal object and a known probe pulse. When time domain ptychography is employed to do pulse reconstruction the pulse can be viewed as the temporal object and the probe can be derived from the unknown temporal object by application of a known transfer function. As such the beam has to be split into two, where one beam is unmodified, referred to as the temporal object beam, and the other beam is modified by application of a spectral transfer function in order to generate a probe pulse. Neither the amplitude or phase of this probe pulse is known, only the applied transfer function and that it is applied to the same spectral amplitude and phase as the temporal object. This allows us to modify the time domain ptychographic iterative engine (TD-PIE) to estimate the amplitude and phase of the probe iteratively, thus the ptychographic iterative reconstruction algorithm for the characterization of temporal pulses (PIRANA) is derived, which allows for reconstruction of the temporal object.

First we describe how we used our double beam temporal shaper (DUBTESP) described in Chapter 4, to implement the split beam geometry to measure the required intensity spectrograms. We also explain how this optical system is similar to SHG-FROG and how this allowed us to easily implement SHG-FROG measurements which we could use to compare and verify the results from our PIRANA. Next we explain the modification to the reconstruction algorithm after which we highlight some of the measurement characteristics and advantages.

6.1 Measurement of spectrograms

Intensity spectrograms have to be measured and these phase-less measurements are then fed to our PIRANA and the SHG-FROG in order to recover said phase, here we explain how our DUBTESP was implemented to record the respective intensity spectrograms required for both iterative reconstruction algorithms.

In the following discussions, functions and their spectral domain representations are implied by the argument of the function containing the temporal variable t for the tempo-

ral domain and the angular frequency ω for the spectral domain, for example $H(t)$ would be the definition of a function in the temporal domain and $H(\omega)$ would be the same function but represented in the spectral domain. Going from the temporal to the spectral domain and back, the standard Fourier and inverse Fourier transforms are applied. Further it is assumed that the reader knows that multiplication in the spectral domain implies convolution in the temporal domain and convolution in the spectral domain implies multiplication in the temporal domain.

The basic scheme to measure an intensity spectrogram for input into PIRANA is illustrated in Fig. 6.1. The unknown input pulse is divided into two replica by a beam splitter such that one beam is transmitted and the other reflected. The reflected replica propagates via a suitable arrangement of mirrors to the BBO crystal and the transmitted replica passes a bandpass filter and is subsequently delayed in time by a suitable arrangement of mirrors before propagating to the BBO crystal. The non-collinear propagating replicas are focused in a non-linear (BBO) crystal and the emerging sum-frequency light is analysed by a spectrometer. Thus, the only physical difference between the optical set-up used to

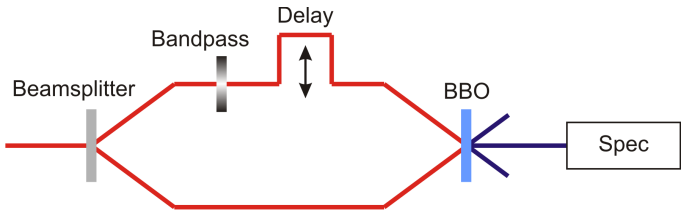

Figure 6.1: Schematic illustrating the idea of the implementation to demonstrate pulse reconstruction using time domain ptychography.

measure the intensity spectrograms for processing by our PIRANA and a standard second harmonic FROG is the spectral bandpass filter which would be left out in a SHG-FROG set-up.

In order to vary all parameters in the most flexible way we decided to demonstrate the principle with our DUBTESP set-up, see Chapter 4, as it allows for individually tailoring both replica of the incident pulse. Just as a beam splitter would result in two replicas of the input pulse, the DUBTESP can apply the same spectral transfer function $H(\omega)$ to pulses from the laser $B(t)$ resulting in duplicate programmable temporal object functions given by

$$E(\omega) = \frac{1}{\sqrt{2}} B(\omega) H(\omega) \tag{6.1.1}$$

Application of a spectral filter $T(\omega)$ in order to generate the time delayed probe pulse $P(t)$ in the probe arm of the DUBTESP set-up, as required by the PIRANA, is done by further multiplication of a time delay spectral transfer function $\exp(\mathrm{i}[\omega - \omega_0]t_n)$ with the spectral filter and the spectral transfer function used to generate the temporal object $H(\omega)$ as given by

$$P(\omega) = E(\omega) T(\omega) \mathrm{e}^{\mathrm{i}(\omega-\omega_0)t_n} \tag{6.1.2}$$

where ω_0 is the carrier frequency of the laser. A sequence of time delayed spectra are recorded denoted by the integer $n = 1..N$ to cover the temporal range required. The

temporal range starts at $t_1 = t_{\text{start}}$ and ends at $t_N = t_{\text{start}} + N\Delta t$. In the case of the SHG-FROG measurements where no spectral filter is present in the probe arm of the set-up only a time delay transfer function is additionally applied to the probe beam given by

$$P(\omega) \quad = \quad E(\omega)\mathrm{e}^{\mathrm{i}(\omega-\omega_0)t_n}. \tag{6.1.3}$$

Just for clarity it is emphasized again that the respective reconstruction algorithms are employed to recover the lost phase in the measured intensity spectrograms after which it is convenient to know what the temporal probes and objects should look like in order to readily compare how well the reconstructed phase compares to theoretical calculation.

A selection of temporal pulses were measured in both regimes, PIRANA and SHG-FROG, by application of the required transfer functions, the light from which are subsequently focused to a 100 µm thick BBO crystal where the exit field, i.e. the product field, is produced through sum-frequency generation in our DUBTESP set-up. The resulting spectra are centered at 400 nm and are analysed by a spectrometer covering the range of 300 nm to 545 nm with a resolution of 0.18 nm.

For the purpose of simplification of the rest of the discussion we will refer to the different aspects of the optical system in terms of Fig. 6.1 since it is enough to know how we emulated this optical system with our DUBTESP set-up. As such with reference to Fig. 6.1, the input pulse $E_{\mathrm{i}}(t)$ is seen as whatever the duplicate programmed pulse shape is and can be considered as if incident on the beam splitter, thus $E_{\mathrm{i}}(t) = B(t) \circledast H(t)$ or $E_{\mathrm{i}}(\omega) = H(\omega)B(\omega)$. The unaltered 'temporal object' is referred to as the transmitted pulse after the beam splitter and is $E(t) = 1/\sqrt{2}E_{\mathrm{i}}(t)$. The reflected pulse as explained is realised by application of an identical transfer function to the one which results in the 'temporal object' in the probe arm of the DUBTESP set-up and as such is given by $E(t)$. In the case of SHG-FROG a further time delay can be applied $P(\omega) = E(\omega)\exp(\mathrm{i}[\omega - \omega_0]t_n)$ to the reflected pulse or in the case of the PIRANA the transfer function of the transmission filter and a time delay by application of the relevant transfer functions $P(\omega) = E(\omega)T(\omega)\exp(\mathrm{i}[\omega - \omega_0]t_n)$.

6.2 Reconstruction using PIRANA

As mentioned we derived PIRANA from the TD-PIE in order to solve the additional constraint of having to reconstruct the probe pulse as it is unknown. The modification to the algorithm is necessary due to the probe being derived from the 'unknown', (unknown from the perspective of the measured intensity spectrogram), input pulse after reflection by application of a filter. As such an extra step needs to be added to the TD-PIE in order to also reconstruct the probe pulse. The added step updates the probe pulse with the reconstructed spectral amplitude and phase before application of the transfer function of the transmission filter as is illustrated in Fig. 6.2.

In order to understand how the probe pulse is updated consider: As mentioned the input pulse $E_{\mathrm{i}}(t)$ is split into two replicas each identical to the input pulse with half the intensity, these are the transmitted pulse and the reflected pulse both referred to as $E(t)$ since they are identical. The probe pulse $P(t)$ is derived from the reflected pulse by application of the spectral transfer function of the filter $T(\omega)$ and a temporal delay formally described in the spectral domain by

$$P(\omega) \quad = \quad E(\omega)T(\omega)\mathrm{e}^{\mathrm{i}(\omega-\omega_0)t_n} \tag{6.2.1}$$

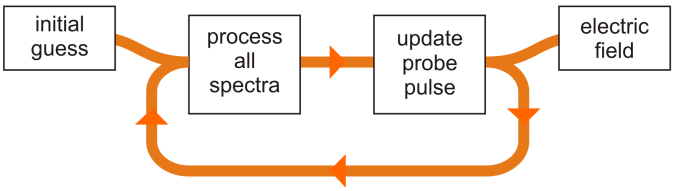

Figure 6.2: The addition of a step to update the probe pulse is showed which enables the pulse reconstruction.

where ω_0 is the carrier frequency of the laser. The task is to determine the unknown electric field of the input pulse $E_{\mathrm{i}}(t)$ from an intensity spectrogram which consists of a sequence of spectra $S(\omega, t_n)$ recorded at different time delays t_n of the probe pulse $P(t)$ by multiplication of said probe pulse with the transmitted pulse $E(t)$.

As a starting point for the retrieval algorithm, we assume for both the initial electric field $E_1(t)$ and the initial probe pulse $P_1(t)$ the inverse Fourier transform of the spectral bandpass filter $T(\omega)$. In every iteration j all measured spectra n are processed. The algorithm calculates the exit field $G_n(t, t_n)$ for a particular time delay t_n of the probe pulse $P_j(t - t_n)$ and the current estimate of the electric field $E_n(t)$ of the pulse. Before proceeding with the next iteration j we update the probe pulse according to

$$P_{j+1}(t - t_n) \quad = \quad \mathscr{F}^{-1}\left\{E_N(\omega)T(\Omega)\mathrm{e}^{\mathrm{i}(\omega-\omega_0)t_n}\right\}. \tag{6.2.2}$$

The best approximation to the actual input pulse appears typically after only a few iterations j under ideal conditions i.e when high signal to noise measured intensity spectrograms are fed to the PIRANA.

Before performing any experiments we ran extensive simulations with the aim to identify the optimal experimental parameters, i.e. the bandpass filter, the time delay increment Δt, and the number of spectra to record, as well as the optimal reconstruction parameters, i.e. α and β.

We found that the bandpass filter should be centered at the carrier frequency of the laser and its width should be less than half the bandwidth of the laser. Smaller widths yield faster convergence, however, at the expense of signal strength. The spectral width of the bandpass then determines the full width at half maximum of the illumination pulse, i.e. FWHM$\{P(t)\}$. The time increment Δt should be approximately $0.5 \cdot$ FWHM$\{P_1(t)\}$. At this point it is important to note that the time delay is related to the temporal duration of the illumination pulse and not determined by the sampling of the spectrogram, as in the case for example of SHG-FROG. Conversely, the temporal resolution is determined by the largest spectral side-bands which can be detected with a sufficient SNR. Spectra should be recorded for as many time delays as signal can be detected.

The trends for α and β were found to be similar to time domain ptychography as discussed in Chapter 5 section 5.2. In the reconstruction the choice of α is determined mostly by the signal-to-noise ratio (SNR) and β by the illumination pulse duration and the time delay. A suitable value for α was determined by analysing the RMS error (RMS refers to the root mean square difference between theoretical and reconstructed spectrogram) for sets of simulated noisy spectra as a function of $\alpha \in [0 \ldots 1]$ and the SNR. For a measured SNR of > 500, $\alpha \approx 0.2$ leads to the smallest RMS. Similarly, the value for $\beta \approx 0.5$ was determined by analyzing the RMS error as function of $\beta \in]0 \ldots 1]$ and the ratio of the

illumination pulse duration $\Delta t/\mathrm{FWHM}\{P(t)\}$. We would like to emphasize that α as well as β can be varied within a wide range of values, the final result only changes by a negligible amount, however, the rate of convergence may slow down.

6.3 Comparison of pulse reconstruction

Since the set-up is closely related to a SHG-FROG arrangement, we compare our results to those obtained by a SHG-FROG. All measurements presented hereafter used the following parameters. The bandpass filter was programmed to have a rectangular spectral transmission characteristic with a width of 3 nm centered at 800 nm. The delay time increment of the probe pulse was $\Delta t = 300$ fs and 11 spectra were recorded as the intensity spectrogram for to be fed to our PIRANA and for SHG-FROG the auto-correlation was done using temporal increments of 20 fs over the required temporal range. For the reconstruction we used $\beta = 0.5$ and $\alpha = 10^{-3}$ in the case of PIRANA and commercially available software for the SHG-FROG reconstructions.

First we show that the respective retrieval algorithms perform adequately by calculating a spectrogram from the reconstructed pulse shapes. In order to do this we generate a relatively complicated temporal pulse which results in temporal replicas by application of the spectral transfer function,

$$H(\Omega) \quad = \quad \mathrm{e}^{\mathrm{i}A\sin(\Omega\tau+\varphi)} \tag{6.3.1}$$

defined around the carrier frequency $\Omega = \omega - \omega_0$. Four intensity spectrograms were measured for input into each of the reconstructed modalities, namely SHG-FROG and PIRANA. In all cases we used Eq. 6.3.1 with parameters $A = 2.4$, $\tau = 350$ fs and $\varphi = 0, \pi/2, \pi, 3\pi/2$. The results are shown in Fig. 6.3. In each case the measured intensity spectrogram is shown with its reconstructed spectrogram below for comparison. The top two rows shows the results for SHG-FROG and the bottom two rows shows the results for PIRANA. In both cases excellent agreement between the reconstructed and the measurements are seen and we note that the asymmetry of the PIRANA measurements allows for visual distinction between phases with opposite sign in contrast to the SHG-FROG results.

Next we explicitly show by analysis of a set of intensity spectrograms that our PIRANA methodology is capable of unambiguously retrieving the sign of the phase of the pulse in comparison to SHG-FROG which can not. This is done by application of a quadratic phase transfer function

$$H(\Omega) = \mathrm{e}^{\mathrm{i}a\Omega^2} \tag{6.3.2}$$

to the input pulse, where $\Omega = \omega - \omega_0$. For our measured set of intensity spectrograms we set a in Eq. 6.3.2 to values ranging from -15000 fs^2 to 15000 fs^2 in increments of 5000 fs^2. Fig. 6.3 shows the results of recovered quadratic spectral phase by SHG-FROG and PIRANA. While SHG-FROG results in the correct values for the quadratic spectral phases, extracted from reconstruction, but random signs our scheme, PIRANA, recovers both the value and the sign correctly which demonstrates the unambiguity of the spectral sign retrieved and unambiguity of the time axis. As a side note, From Fig. 6.3 we see that the pulse has a residual quadratic spectral phase of about a 1000 fs^2.

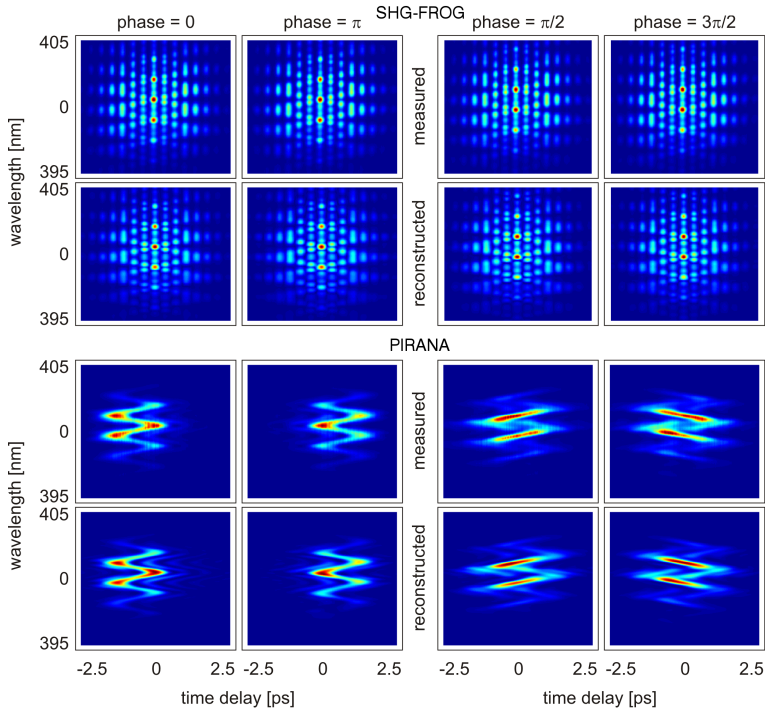

Figure 6.3: Comparison of measured and reconstructed spectrograms for both SHG-FROG and PIRANA demonstrating the symmetric and asymmetric spectrograms measured for SHG-FROG and PIRANA respectively.

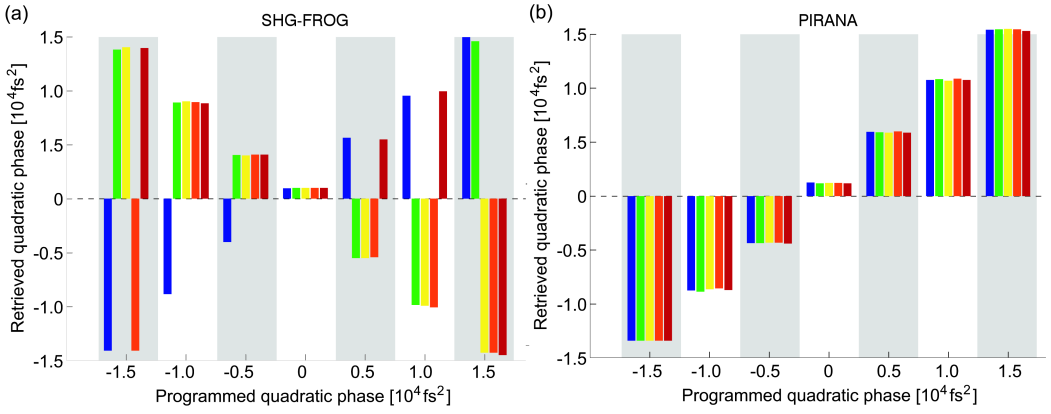

Figure 6.4: Reconstructed high order chirped phase for both SHG-FROG and PIRANA, each colour representing a reconstruction of the respective measured spectrogram, demonstrating that PIRANA has no sign ambiguity.

Next, we analyse different combinations of second, third, and fourth order phase contributions by application of the transfer function

$$H(\Omega) \quad = \quad e^{i(\phi_2\Omega^2+\phi_3\Omega^3+\phi_4\Omega^4)} \tag{6.3.3}$$

defined around the carrier frequency ω_0 as $\Omega = \omega - \omega_0$ to the input pulse with PIRANA and SHG-FROG. The results of both retrievals are summarized in table 6.1. The second,

third, and fourth order phases were $\phi_2 = \pm 10^4$ fs^2, $\phi_3 = \pm 2.5 \cdot 10^5$ fs^3, and $\phi_4 = \pm 5 \cdot 10^6$ fs^4, respectively. When disregarding the sign issue, we find that both, FROG and

Table 6.1: Columns 1 to 3 show the programmed second, third, and fourth order phases. The numbers given (−1, 0 , 1) have to be multiplied by 10^4 fs^2, $2.5 \cdot 10^5$ fs^3, and $5 \cdot 10^6$ fs^4 for the second, third, and fourth order phase, respectively. Columns 4 to 6 show results of the FROG retrieval and columns 7 to 9 results from the PIRANA scheme.

target			FROG			PIRANA		
ϕ_2	ϕ_3	ϕ_4	ϕ_2	ϕ_3	ϕ_4	ϕ_2	ϕ_3	ϕ_4
0	1	0	0.05	1.18	-0.18	0.05	1.15	-0.13
0	0	1	0.01	-0.09	0.97	0.02	0.07	0.84
1	0	-1	0.93	0.04	-0.90	0.90	-0.01	-0.90
1	1	-1	0.81	0.83	-0.85	0.94	1.04	-0.75
-1	-1	1	-0.90	-1.12	1.09	-1.03	-1.01	0.88
1	-1	-1	1.08	-0.83	-0.93	1.05	-0.94	-1.03

PIRANA, produce correct values for the six different combinations of $\phi_{1,2,3}$ tested.

Lastly we investigated a sinusoidal phase modulation to compare the extracted phase from SHG-FROG to our reconstruction modality. In order to do this we again apply the spectral transfer fucntion

$$f(\omega) \quad = \quad e^{iA\sin(\Omega\tau+\varphi)}, \tag{6.3.4}$$

centered around the carrier frequency ω_0 such that $\Omega = \omega - \omega_0$, to the input pulse. Four intensity spectra were recorded for both modalities, namely SHG-FROG and PIRANA using the parameters $A = 2.4$, $\tau = 350$ fs and $\varphi = 0, \pi/2, \pi, 3\pi/2$ in the applied transfer function Eq. 6.3.4. The respective resultant measured intensity spectrograms are fed to the respective algorithms and the spectral phase extracted is plotted in Fig. 6.3. The top

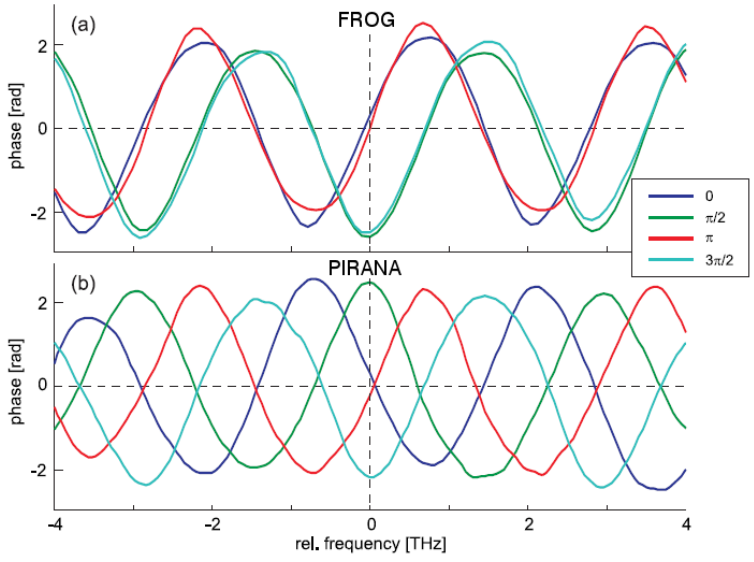

Figure 6.5: Reconstructed phases for both (a) SHG-FROG and (b) PIRANA.

graph shows the phase extracted by SHG-FROG and the bottom graph the phase extracted by our PIRANA methodology. We see that FROG can distinguish between a sinusoidal ($\varphi = 0$) and a co-sinusoidal ($\varphi = \pi/2$) oscillation but not between two sinusoidal phase oscillations with opposite sign ($\varphi = 0$ and $\varphi = \pi$). The PIRANA modality, however, can distinguish between all four oscillatory phases.

In summary, our scheme has a number of distinct advantages. 1) In contrast to a SHG-FROG there is no time ambiguity in the measurement, that is, not only the magnitude of a phase modulation but also its sign can be unambiguously retrieved. 2) Only a few spectra (on the order of 5 to 20) have to be recorded for PIRANA. 3) The small number of spectra also results in an extremely fast convergence of the retrieval algorithm. 4) As mentioned above the time delay increment Δt is not related to the desired temporal resolution or the wavelength sampling of the spectrometer, but only to the duration of $P(t)$. The only drawback is that the signal strength is somewhat lower because the spectral bandpass filter in one arm lowers the intensity of the pulse.

In conclusion, we have demonstrated a new modality for ultrashort pulse reconstruction which is based on a retrieval algorithm derived from ptychography. It converges extremely fast and reliably and can be easily extended to other non-linear processes, such as DFG etc. Further the optical set-up is so close to SHG-FROG that one can easily convert said setup to a PIRANA by inserting a transmission filter chosen as described with a known spectral transmission response.

7

Conclusion

We expanded on the analysis of the application of blazed gratings for spatial beam shaping using 2D-SLMs to find an expression which explains how the application of a 2D-SLM in a 4f-shaper can be realised. We then built a versatile optical set-up using 2D-SLMs which allows us to individually tailor two beams for various measurements. Next we extended ptychography, a spatial lens-less imaging technique, to the time domain for the first time and have shown that the technique can be used to reconstruct, relatively quickly, arbitrary temporal objects with a resolution dependent on the bandwidth of the spectrometer rather than the probe pulse duration without any sign ambiguity in the recovered phase. We then proceeded to extend the technique, for the first time, to pulse characterization using a set-up very similar optically to a second harmonic generation frequency resolved optical gating set-up, allowing for easy conversion from the one to the other, again showing the extended technique is capable of quick characterization of arbitrary temporal pulse shapes without any phase ambiguity.

In future, several possibilities exist to extend this work. The methodology is envisaged to be specifically valuable for a number of time-resolved pump-probe spectroscopy schemes. Typically, an ultrashort pump pulse triggers a material response 'object' function which is then probed by another ultrashort probe pulse. Depending on the type of spectroscopy the probe pulse may have a different wavelength than the pump or may even be an extremely broad super-continuum as in transient absorption. Irrespective of the specific type of spectroscopy, the probe pulse duration needs to be shorter than the fastest dynamical feature to be measured. With the time domain ptychography probing scheme the requirement of a sufficiently short probe pulse is relaxed. Moreover, the time delays required to raster scan the material response (object function) can be orders of magnitudes larger than in traditional pump-probe spectroscopy. This is especially useful when probing requires ultrashort pulses in regions where they are not readily available, for example in the UV. Another advantage, albeit more technical in nature, is that beam delivery systems no longer need to be extremely broadband, e.g. dielectric mirrors, wave plates etc., which are often expensive and difficult to produce. A longer probe pulse may also generate less coherent artefacts, making data interpretation easier. For example, in homodyne transient grating spectroscopy the generated third order polarization can be expressed as

$$\mathcal{P}^{(3)}(\vec{k},t) = -P(t) \int_0^\infty \mathrm{d}t_1 \, \chi^{(3)}(t_1) \; \left|E_\mathrm{p}(t+\tau-t_1)\right|^2$$

with the time delay τ between the pump pulse $E_\mathrm{p}(t)$ forming the transient grating and the

probe pulse $P(t)$. Time domain ptychography would allow to reconstruct the convolution of the pump pulse and the third order material response without the need of a short probe pulse. If the pump pulse is known from a separate measurement or assumed to be impulsive, the material response can be readily extracted.

Although the ptychographic reconstruction of transient phenomena in the UV, VIS, or IR regime is of interest, the largest potential is expected to unfold in the X-ray regime. With the emergence of spatially and temporally coherent pulsed X-ray sources the scheme proposed here would allow for new time-resolved imaging modalities. Both optical pump/X-ray probe and X-ray pump/X-ray probe schemes are conceivable, the latter however requires a nonlinear interaction with several X-ray photons. The shortest X-ray pulses reported to date are 3 fs [55] which would allow time domain ptychography to reconstruct ultrafast phenomena in the attosecond range. Most of the advantages outlined above also apply here. Furthermore, if time domain ptychography is combined with spatial ptychography, the emerging concept will pave the road towards time-resolved imaging, i.e. time-resolved imaging of aperiodic atomic-scale objects on relevant time scales. These are femtoseconds for molecular or attoseconds for electronic dynamics and thus, well within reach.

Further refinement of the pulse characterization ptychographic reconstruction method could be investigated in order to simplify the optical set-up such that it could become a simple and accurate diagnostic tool to implement in ultrashort laser labs.

Appendices

A

Mathematical derivations

A.1 Temporal envelope calculation

Consider the Fourier transform for which extensive transform pair tables exist

$$F(X) = \int_{-\infty}^{\infty} f(x)\mathrm{e}^{-ixX}dx \tag{A.1.1}$$

and the optical Fourier transform, where f_u denotes the input field at the focal plain a distance f in front of the lens, F_v denotes the output field at the focal plane a distance f behind the lens and $C = \frac{A}{\mathrm{i}\lambda f}$,

$$F_\mathrm{v}(X) = C\int_{-\infty}^{\infty} f_\mathrm{u}(x)\mathrm{e}^{-i\gamma xX}dx \tag{A.1.2}$$

and note that the main difference is the phase scaling factor $\gamma = \frac{2\pi}{\lambda f}$. By substitution of $y = \gamma x$, $dx = \frac{dy}{\gamma}$ and $x = \frac{y}{\gamma}$ into Eq. A.1.2

$$F_\mathrm{v}(X) = \frac{C}{\gamma}\int_{-\infty}^{\infty} f_\mathrm{u}\left(\frac{y}{\gamma}\right)\mathrm{e}^{-iyX}dy \tag{A.1.3}$$

the form of the optical Fourier transform is such that existing Fourier transform tables can be easily applied with the main difference being the function scaling factor γ.

One can use the Fourier transform pair for a scaled function

$$f(\alpha u) \overset{\mathscr{F}}{\longleftrightarrow} \frac{1}{|\alpha|}F\left(\frac{U}{\alpha}\right) \tag{A.1.4}$$

substituting $\alpha = \frac{1}{\gamma}$, $U = X$, $u = y$ and $x = \frac{y}{\gamma}$ to find an expression which can be used to express standard Fourier transforms as optical Fourier transforms,

$$f(x) \overset{\mathscr{F}_\mathrm{opt}}{\longleftrightarrow} CF(\gamma X). \tag{A.1.5}$$

One can use the relation in Eq. A.1.5 to write the optical Fourier transform for a Guassian input function,

$$\exp\left(\frac{-x^2}{2\sigma_\mathrm{x}^2}\right) \overset{\mathscr{F}_\mathrm{opt}}{\longleftrightarrow} C\sigma_\mathrm{x}\sqrt{2\pi}\exp\left(\frac{-\sigma_\mathrm{x}^2\gamma^2X^2}{2}\right). \tag{A.1.6}$$

We can use the spectral calibration axis to convert between spectrum and space in the back focal plane of the lens with $\omega = \frac{\Delta\omega}{\Delta X}X$ rad, thus we can calculate the Gaussian width

σ_f of any spectral component using the optical Fourier transform and then converting to frequency. If we consider that the SLM in combination with a transfer function is given by H_{TRF} and the Gaussian illumination of each spectral component is given by F_G then we can write an expression for the illumination on the SLM as

$$F(\omega) = \int_{-\infty}^{\infty} F_G(\omega - \omega_0) H_{TRF}(\omega_0) d\omega_0 \tag{A.1.7}$$

which can be recognised as a convolution. Thus we can multiply the temporal function $F_G(t)$ with the temporal transfer function $H_{TRF}(t)$. To calculate the spectral width of the Gaussian focus in frequency we use Eq. A.1.6 and solve for the spectral Guassian width σ_f,

$$\begin{aligned} \sigma_f &= \frac{1}{\gamma \sigma_x} \cdot \frac{\Delta\omega}{\Delta X} \\ &= \frac{\lambda f}{\sigma_x 2\pi} \cdot \frac{\Delta\omega}{\Delta X} \\ &= 0.930 \text{ rad/ps} \end{aligned}$$

where $\sigma_x = 2$ mm, $f = 130$ mm, $\lambda = 800$ nm, $\Delta\omega = 0.898$ rad/ps and $\Delta X = 8\,\mu$m. The Fourier transform could be used to get the temporal width of the spectral Gaussian function.

$$\begin{aligned} \sigma_t &= \frac{1}{\sigma_f} \\ &= \frac{2\pi}{0.930 \text{ rad/ps}} \\ &= 67.6 \times 10^2 \text{ fs} \end{aligned}$$

A.2 Grating pair phase analysis

Here we calculate the modification of the spectral phase for the grating pair implemented in our double beam temporal pulse shaper. The grating equation Eq. 2.2.1 can be simplified to find the propagation angle $\beta(\lambda)$ of wavelengths for our 10 nm source with

$$\beta(\lambda) \approx \frac{\lambda}{p} \tag{A.2.1}$$

where λ is the wavelength and p is the pitch of the grating and the approximation is made that $\sin\beta \approx \beta$. Now the optical path of each spectral component $L(\lambda)$ can be calculated for the case where the output is aligned with the central wavelength λ_0 in the first diffraction order using

$$L(\lambda) = \frac{D}{\cos\frac{\lambda - \lambda_0}{p}} \tag{A.2.2}$$

where D is the distance between the grating pair. The phase of each wavelength $\phi(\lambda)$ can then calculated by dividing by the respective wavelength,

$$\phi(\lambda) = \frac{L(\lambda)}{\lambda} \tag{A.2.3}$$

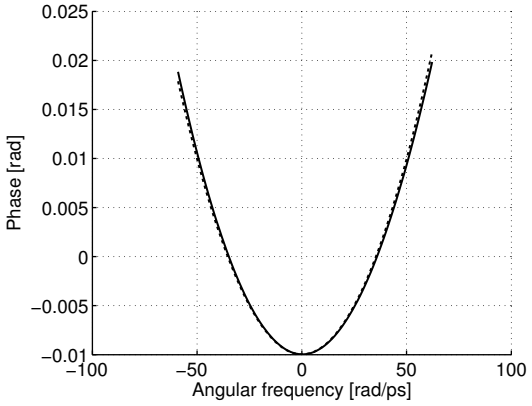

Figure A.1: Graph of the quadratic phase fit to extract the amount of quadratic phase introduced by our grating pair. The calculation is indicated by the solid line and the fit is indicated by the dashed line.

the result from which can be used to fit a polynomial to extract the spectral phase distortion. The resultant plot and fit of this calculation is shown in Fig. A.1. The parameter extracted from the polynomial fit when p =160 µm, λ_0 =800 nm and D = 45 cm is as follows: 7.97 fs^2, -3.39 fs^3, 1.43 fs^4.

B

Reconstructions

Here we show, in Figs. B1-9, reconstructions for various temporal object functions. In all cases the reconstructions converged in 500 iterations with reconstruction parameters $\beta = 0.4$, $\alpha = 0.1$ and $\Delta t = 200$ fs. In each subsequent figure the measured intensity spectrogram is shown as an inlay at the top left and below it the intensity spectrogram calculated from the reconstructed temporal object for comparison. The reconstructed temporal object is plotted along with its phase with a red and blue dashed line respectively and the theoretically calculated temporal object as a solid red and blue line for comparison.

For spectral slice probe pulses of 6 nm and 3 nm the measured intensity spectrograms were used as is, but in the case of the 1.5 nm recordings it was necessary to apply some filtering before using the measured intensity spectrograms as input to the time domain ptychographic iterative engine (TD-PIE).

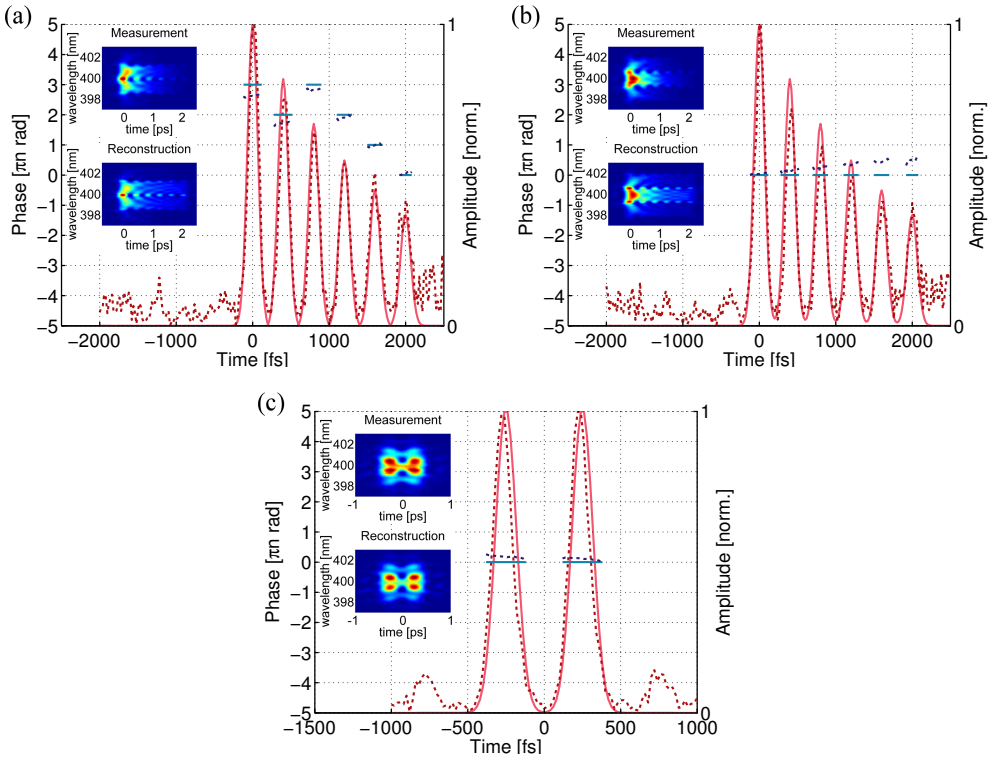

Figure B.1: Reconstructions of temporal object functions measured by application of an amplitude and phase spectral transfer functions probed by a 6 nm spectral slice probe, showing (a) a pulse train with $\tau = 400$, $\gamma = 5$ and $M + 1 = 6$ replicas, (b) an alternating pulse train with $\tau = 400$, $\gamma = 5$ and $M + 1 = 6$ and (c) a double pulse with $\tau = 500$.

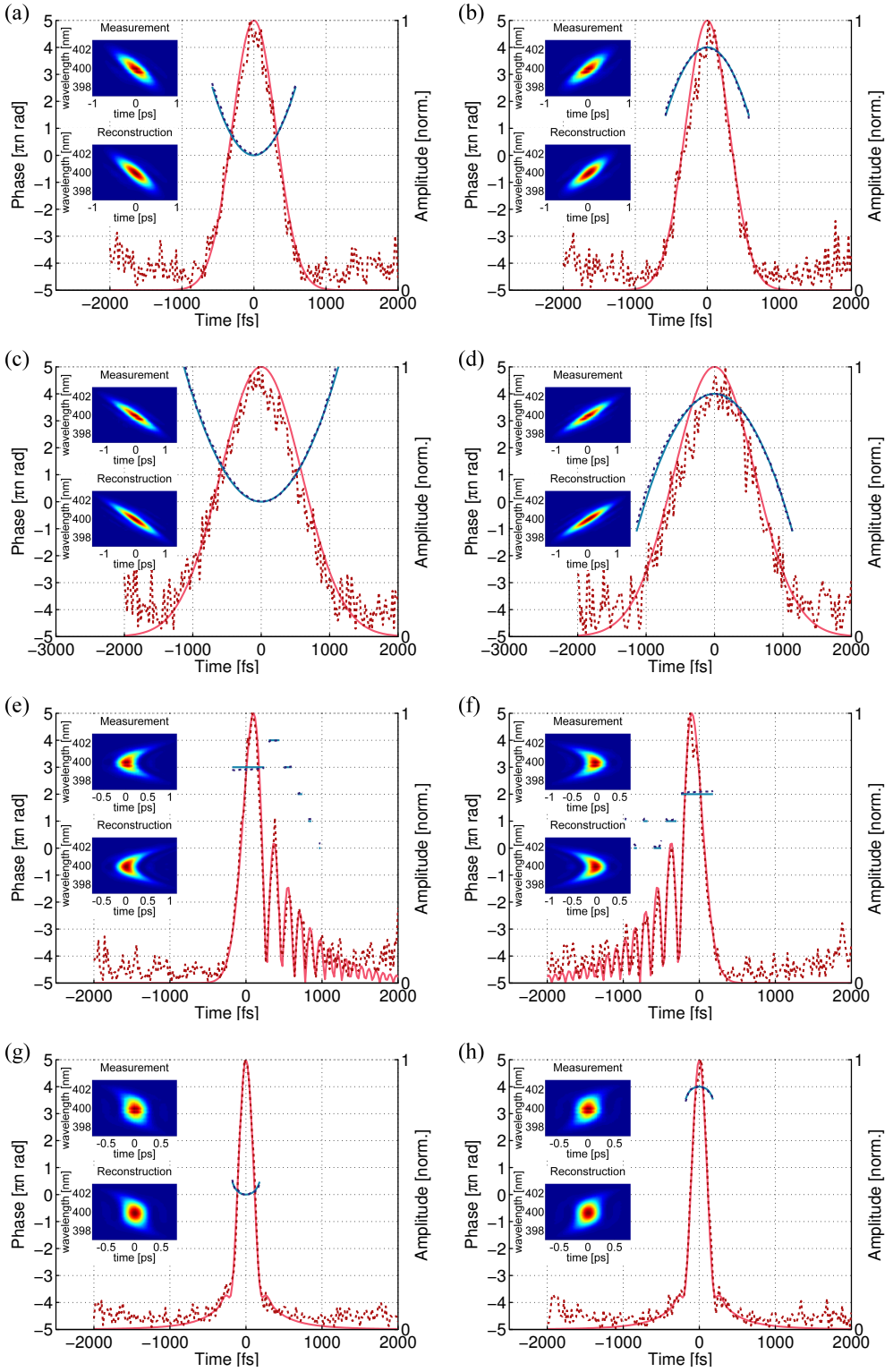

Figure B.2: Reconstructions of temporal object functions measured by application of a polynomial phase spectral transfer functions probed by a 6 nm spectral slice probe, showing (a) quadratic spectral phase with $a = 10^4$, $b = 0$ and $c = 0$, (c) quadratic spectral phase with $a = -10^4$, $b = 0$ and $c = 0$, (c) quadratic spectral phase with $a = 2 \times 10^4$, $b = 0$ and $c = 0$, (d) quadratic spectral phase with $a = -2 \times 10^4$, $b = 0$ and $c = 0$, (e) third order spectral phase with $a = 0$, $b = 5 \times 10^5$ and $c = 0$, (f) third order spectral phase with $a = 0$, $b = -5 \times 10^5$ and $c = 0$, (g) fourth order spectral phase with $a = 0$, $b = 0$ and $c = 5 \times 10^6$ and (h) fourth order spectral phase with $a = 0$, $b = 0$ and $c = -5 \times 10^6$.

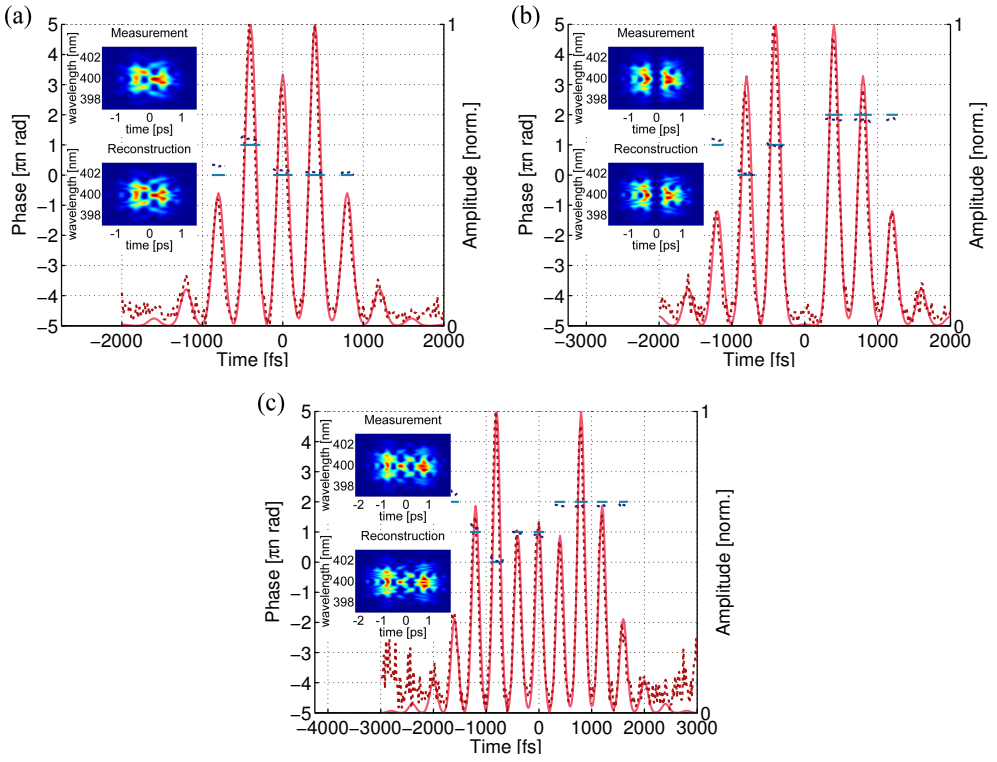

Figure B.3: Reconstructions of temporal object functions measured by application of a sinusoidal phase spectral transfer function probed by a 6 nm spectral slice probe, showing (a) pulse replicas generated with $A = \pi/2$ and $\tau = 400$ fs (b) pulse replicas generated with $A = 2.4$ and $\tau = 400$ fs and (c) pulse replicas generated with $A = \pi$ and $\tau = 400$ fs.

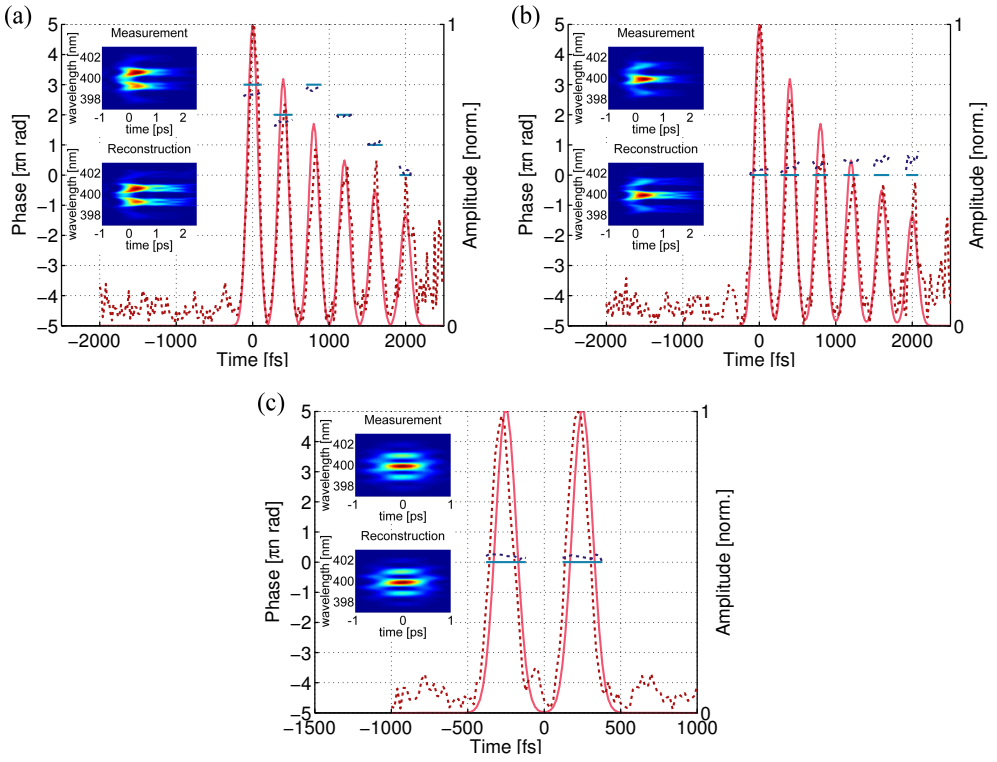

Figure B.4: Reconstructions of temporal object functions measured by application of an amplitude and phase spectral transfer functions probed by a 3 nm spectral slice probe, showing (a) a pulse train with $\tau = 400$, $\gamma = 5$ and $M + 1 = 6$ replicas, (b) an alternating pulse train with $\tau = 400$, $\gamma = 5$ and $M + 1 = 6$ and (c) a double pulse with $\tau = 500$.

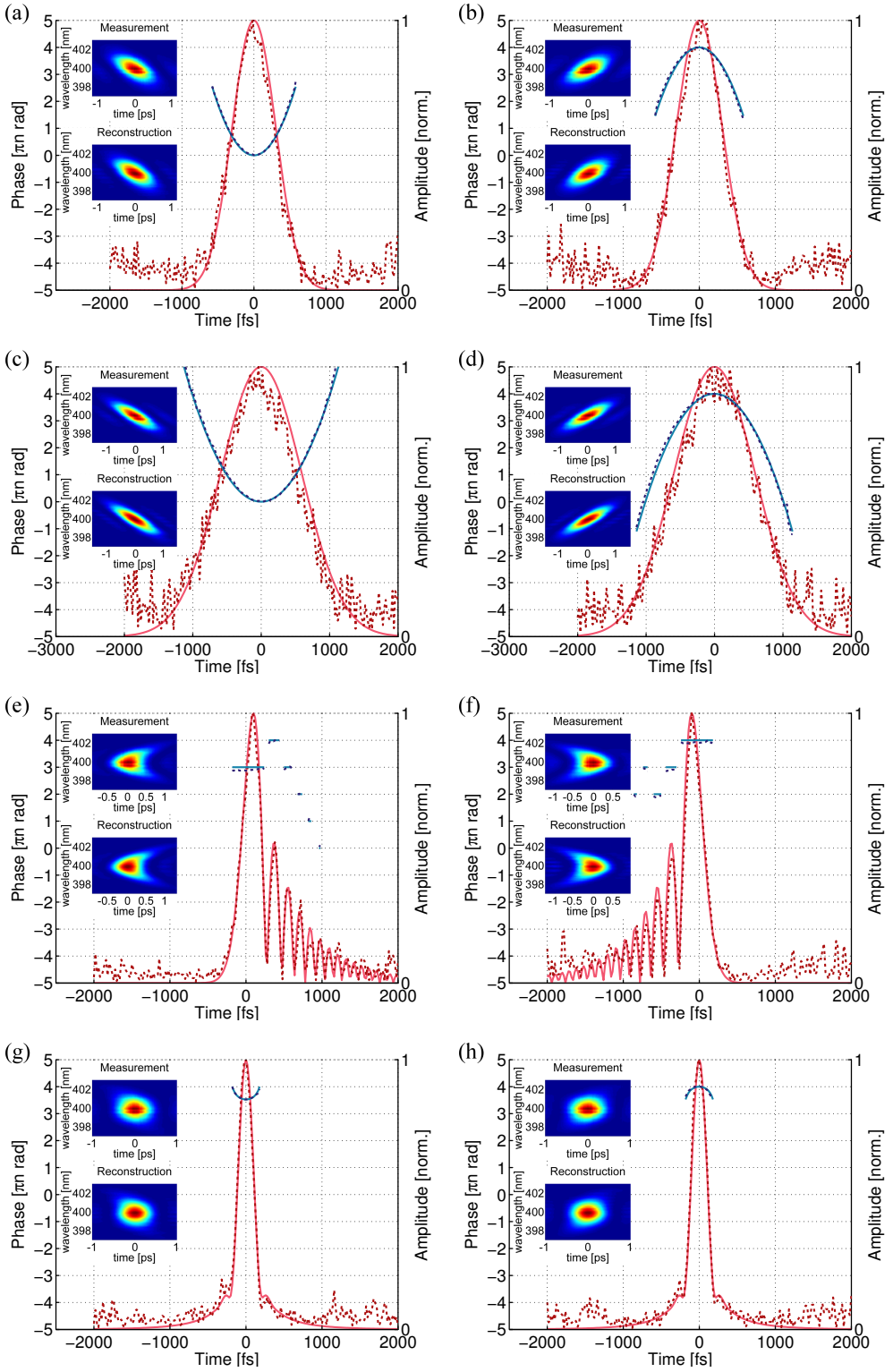

Figure B.5: Reconstructions of temporal object functions measured by application of a polynomial phase spectral transfer function probed by a 3 nm spectral slice probe, showing (a) quadratic spectral phase with $a = 10^4$, $b = 0$ and $c = 0$, (c) quadratic spectral phase with $a = -10^4$, $b = 0$ and $c = 0$, (c) quadratic spectral phase with $a = 2 \times 10^4$, $b = 0$ and $c = 0$, (d) quadratic spectral phase with $a = -2 \times 10^4$, $b = 0$ and $c = 0$, (e) third order spectral phase with $a = 0$, $b = 5 \times 10^5$ and $c = 0$, (f) third order spectral phase with $a = 0$, $b = -5 \times 10^5$ and $c = 0$, (g) fourth order spectral phase with $a = 0$, $b = 0$ and $c = 5 \times 10^6$ and (h) fourth order spectral phase with $a = 0$, $b = 0$ and $c = -5 \times 10^6$.

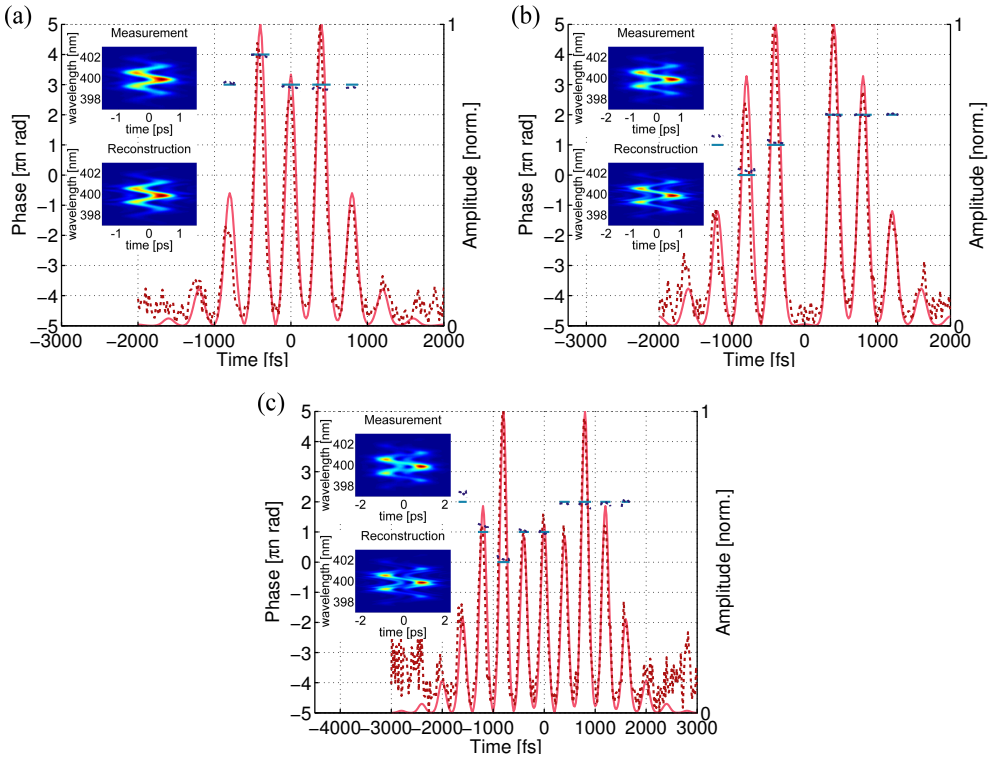

Figure B.6: Reconstructions of temporal object functions measured by application of a sinusoidal phase spectral transfer function probed by a 3 nm spectral slice probe, showing (a) pulse replicas generated with $A = \pi/2$ and $\tau = 400$ fs (b) pulse replicas generated with $A = 2.4$ and $\tau = 400$ fs and (c) pulse replicas generated with $A = \pi$ and $\tau = 400$ fs.

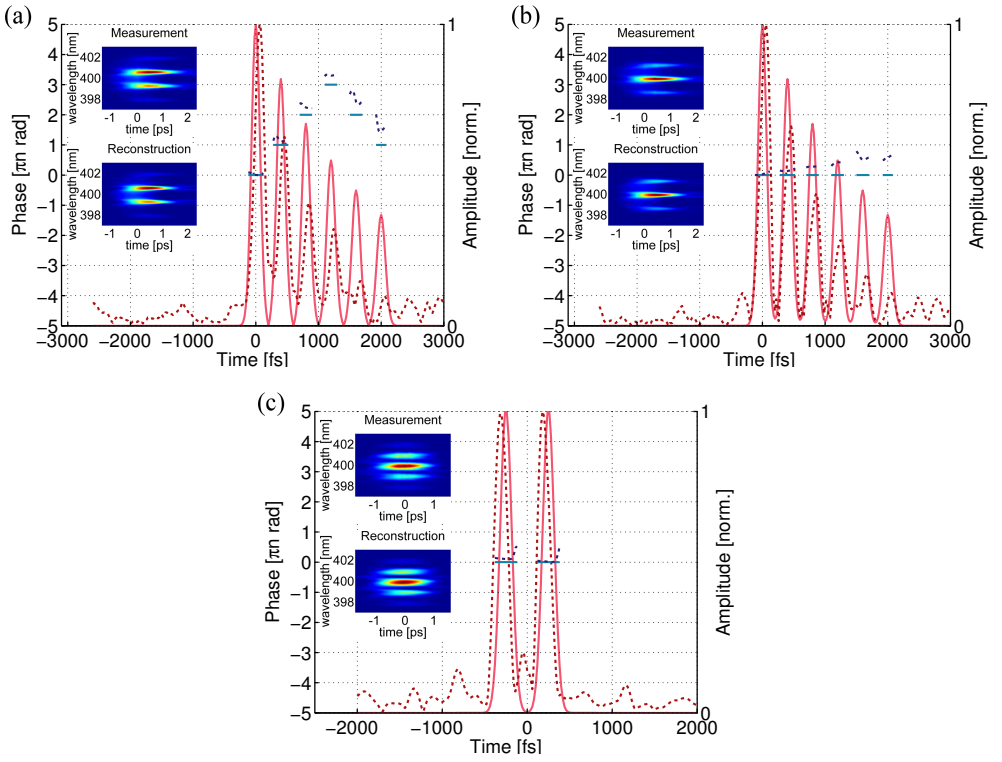

Figure B.7: Reconstructions of temporal object functions measured by application of an amplitude and phase spectral transfer functions probed by a 1.5 nm spectral slice probe, showing (a) a pulse train with $\tau = 400$, $\gamma = 5$ and $M + 1 = 6$ replicas, (b) an alternating pulse train with $\tau = 400$, $\gamma = 5$ and $M + 1 = 6$ and (c) a double pulse with $\tau = 500$.

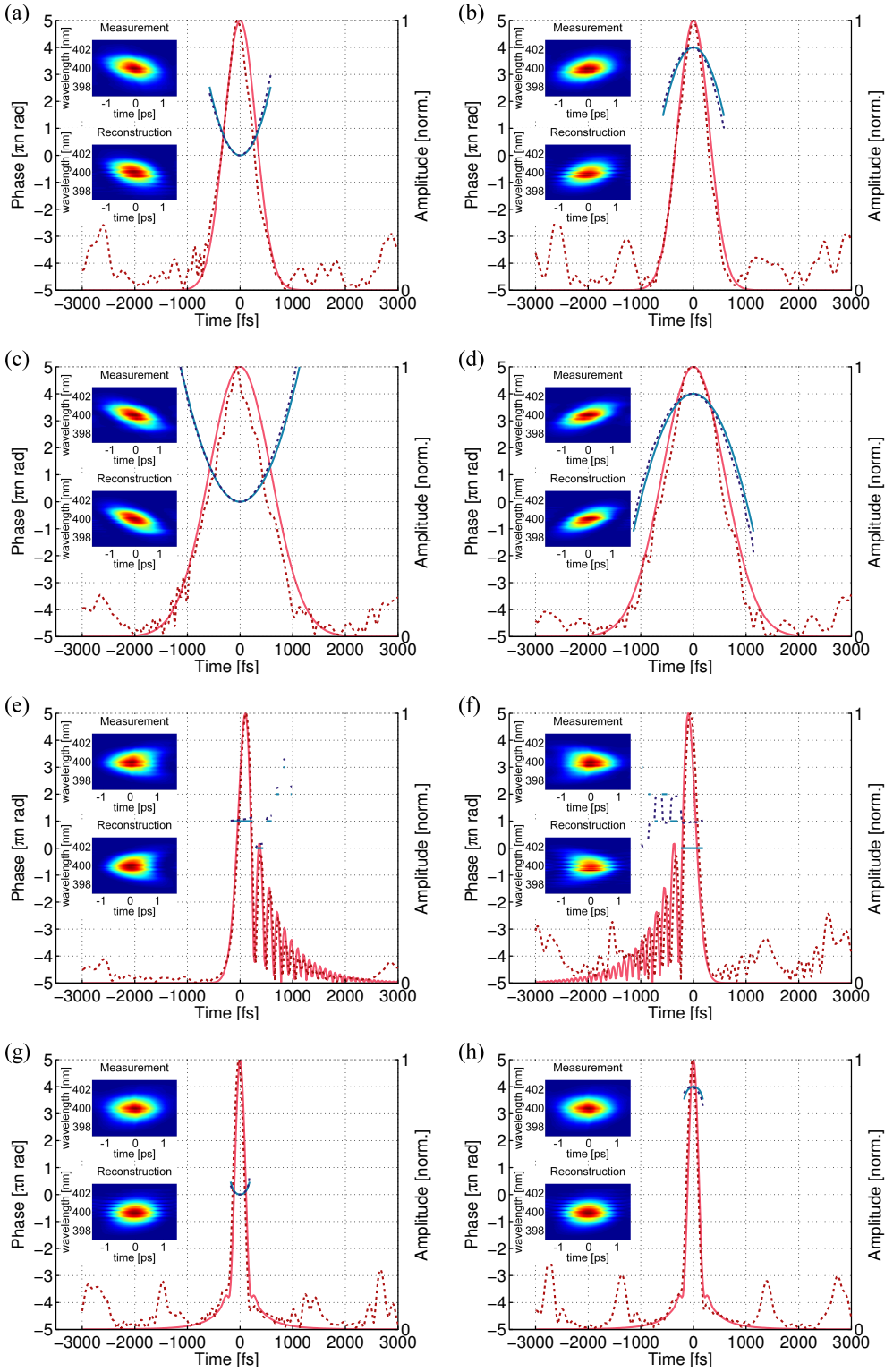

Figure B.8: Reconstructions of temporal object functions measured by application of a polynomial phase spectral transfer function probed by a 1.5 nm spectral slice probe, showing (a) quadratic spectral phase with $a = 10^4$, $b = 0$ and $c = 0$, (c) quadratic spectral phase with $a = -10^4$, $b = 0$ and $c = 0$, (c) quadratic spectral phase with $a = 2 \times 10^4$, $b = 0$ and $c = 0$, (d) quadratic spectral phase with $a = -2 \times 10^4$, $b = 0$ and $c = 0$, (e) third order spectral phase with $a = 0$, $b = 5 \times 10^5$ and $c = 0$, (f) third order spectral phase with $a = 0$, $b = -5 \times 10^5$ and $c = 0$, (g) fourth order spectral phase with $a = 0$, $b = 0$ and $c = 5 \times 10^6$ and (h) fourth order spectral phase with $a = 0$, $b = 0$ and $c = -5 \times 10^6$.

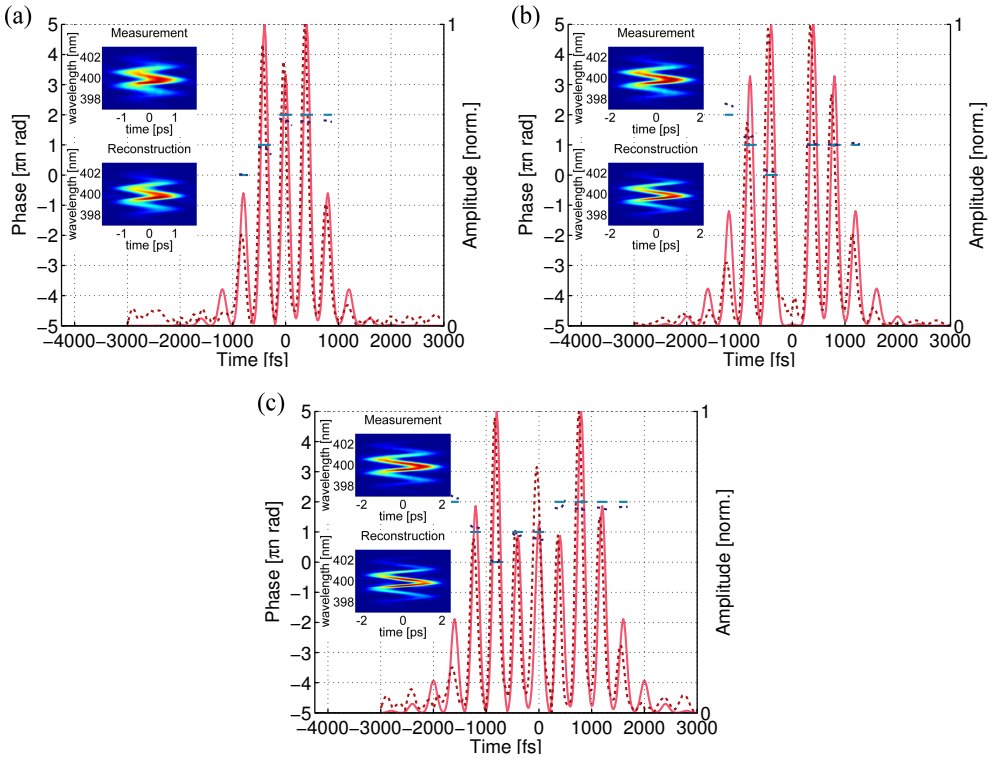

Figure B.9: Reconstructions of temporal object functions measured by application of a sinusoidal phase spectral transfer function probed by a 1.5 nm spectral slice probe, showing (a) pulse replicas generated with $A = \pi/2$ and $\tau = 400$ fs (b) pulse replicas generated with $A = 2.4$ and $\tau = 400$ fs and (c) pulse replicas generated with $A = \pi$ and $\tau = 400$ fs.

List of References

[1] Bradley, D.J. and New, G.H.C.: Ultrashort pulse measurements. *Proceedings of the IEEE*, vol. 62, no. 3, pp. 313–345, 1974.
Available at: http://dx.doi.org/10.1109/proc.1974.9427

[2] Spangenberg, D., Neethling, P., Rohwer, E., Brügmann, M.H. and Feurer, T.: Ptychochronography: Ultrafast lens-less imaging in the time domain. *ArXiv e-prints*, April 2014. 1404.7621.

[3] Spangenberg, D., Rohwer, E., Brügmann, M.H. and Feurer, T.: Ptychographic ultrafast pulse reconstruction. *ArXiv e-prints*, November 2014. 1411.6861.

[4] Spangenberg, D., Dudley, A., Neethling, P.H., Rohwer, E.G. and Forbes, A.: White light wavefront control with a spatial light modulator. *Opt. Express*, vol. 22, no. 11, p. 13870, Jun 2014.
Available at: http://dx.doi.org/10.1364/OE.22.013870

[5] Gerchberg, R.W. and Saxton, W.O.: A practical algorithm for the determination of the phase from image and diffraction plane pictures. *Optik (Jena)*, vol. 35, pp. 237+, 1972.

[6] Fienup, J.R.: Phase retrieval algorithms: a comparison. *Applied Optics*, vol. 21, no. 15, p. 2758, Aug 1982.
Available at: http://dx.doi.org/10.1364/AO.21.002758

[7] Miao, J., Charalambous, P., Kirz, J. and Sayre, D.: *Nature*, vol. 400, no. 6742, pp. 342–344, jul 1999.
Available at: http://dx.doi.org/10.1038/22498

[8] Nugent, K., Peele, A., Chapman, H. and Mancuso, A.: Unique phase recovery for nonperiodic objects. *Phys. Rev. Lett.*, vol. 91, no. 20, nov 2003.
Available at: http://dx.doi.org/10.1103/PhysRevLett.91.203902

[9] Eisebitt, S., Lüning, J., Schlotter, W.F., Lörgen, M., Hellwig, O., Eberhardt, W. and Stöhr, J.: Lensless imaging of magnetic nanostructures by x-ray spectro-holography. *Nature*, vol. 432, no. 7019, pp. 885–888, dec 2004.
Available at: http://dx.doi.org/10.1038/nature03139

[10] Chapman, H.N., Barty, A., Marchesini, S., Noy, A., Hau-Riege, S.P., Cui, C., Howells, M.R., Rosen, R., He, H., Spence, J.C.H., Weierstall, U., Beetz, T., Jacobsen, C. and Shapiro, D.: High-resolution ab initio three-dimensional x-ray diffraction microscopy. *J. Opt. Soc. Am. A*, vol. 23, no. 5, p. 1179, 2006.
Available at: http://dx.doi.org/10.1364/JOSAA.23.001179

[11] Maiden, A.M. and Rodenburg, J.M.: An improved ptychographical phase retrieval algorithm for diffractive imaging. *Ultramicroscopy*, vol. 109, no. 10, pp. 1256–1262, sep 2009.
Available at: http://dx.doi.org/10.1016/j.ultramic.2009.05.012

[12] Greenbaum, A., Luo, W., Su, T.-W., Görös, Z., Xue, L., Isikman, S.O., Coskun, A.F., Mudanyali, O. and Ozcan, A.: Imaging without lenses: achievements and remaining challenges of wide-field on-chip microscopy. *Nat Meth*, vol. 9, no. 9, pp. 889–895, aug 2012.
Available at: http://dx.doi.org/10.1038/nmeth.2114

[13] Marrison, J., Räty, L., Marriott, P. and O'Toole, P.: Ptychography – a label free, high-contrast imaging technique for live cells using quantitative phase information. *Scientific Reports*, vol. 3, aug 2013.
Available at: http://dx.doi.org/10.1038/srep02369

[14] Fienup, J.R.: Phase retrieval algorithms: a personal tour [invited]. *Applied Optics*, vol. 52, no. 1, p. 45, dec 2012.
Available at: http://dx.doi.org/10.1364/AO.52.000045

[15] Hoppe, W.: Beugung im inhomogenen Primärstrahlwellenfeld. III. Amplituden- und Phasenbestimmung bei unperiodischen Objekten. *Acta Crystallographica Section A*, vol. 25, no. 4, pp. 508–514, Jul 1969.
Available at: http://dx.doi.org/10.1107/S0567739469001069

[16] Rodenburg, J., Hurst, A. and Cullis, A.: Transmission microscopy without lenses for objects of unlimited size. *Ultramicroscopy*, vol. 107, no. 2-3, pp. 227–231, feb 2007.
Available at: http://dx.doi.org/10.1016/j.ultramic.2006.07.007

[17] Holler, M., Diaz, A., Guizar-Sicairos, M., Karvinen, P., Faïrm, E., Härkönen, E., Ritala, M., Menzel, A., Raabe, J. and Bunk, O.: X-ray ptychographic computed tomography at 16 nm isotropic 3d resolution. *Scientific Reports*, vol. 4, jan 2014.
Available at: http://dx.doi.org/10.1038/srep03857

[18] McCallum, B. and Rodenburg, J.: Two-dimensional demonstration of wigner phase-retrieval microscopy in the STEM configuration. *Ultramicroscopy*, vol. 45, no. 3-4, pp. 371–380, nov 1992.
Available at: http://dx.doi.org/10.1016/0304-3991(92)90149-E

[19] Hornung, T., Vaughan, J.C., Feurer, T. and Nelson, K.A.: Degenerate four-wave mixing spectroscopy based on two-dimensional femtosecond pulse shaping. *Optics Letters*, vol. 29, no. 17, p. 2052, 2004.
Available at: http://dx.doi.org/10.1364/OL.29.002052

[20] Weber, H.P.: Method for pulsewidth measurement of ultrashort light pulses generated by phase-locked lasers using nonlinear optics. *J. Appl. Phys.*, vol. 38, no. 5, p. 2231, 1967.
Available at: http://dx.doi.org/10.1063/1.1709859

[21] Diels, J.-C.M., Fontaine, J.J., McMichael, I.C. and Simoni, F.: Control and measurement of ultrashort pulse shapes (in amplitude and phase) with femtosecond accuracy. *Applied Optics*, vol. 24, no. 9, p. 1270, 1985.
Available at: http://dx.doi.org/10.1364/AO.24.001270

[22] DeLong, K.W., Trebino, R., Hunter, J. and White, W.E.: Frequency-resolved optical gating with the use of second-harmonic generation. *Journal of the Optical Society of America B*, vol. 11, no. 11, p. 2206, Nov 1994.
Available at: http://dx.doi.org/10.1364/JOSAB.11.002206

[23] Trebino, R.: *Frequency-Resolved Optical Gating: The Measurement of Ultrashort Laser Pulses*. Springer US Imprint Springer, Boston, MA, 2000. ISBN 978-1-4615-1181-6.

[24] Chilla, J.L.A. and Martinez, O.E.: Direct determination of the amplitude and the phase of femtosecond light pulses. *Optics Letters*, vol. 16, no. 1, p. 39, Jan 1991.
Available at: http://dx.doi.org/10.1364/OL.16.000039

[25] Iaconis, C. and Walmsley, I.: Spectral phase interferometry for direct electric-field reconstruction of ultrashort optical pulses. *Optics Letters*, vol. 23, no. 10, p. 792, May 1998.
Available at: http://dx.doi.org/10.1364/OL.23.000792

[26] Nicholson, J.W., Jasapara, J., Rudolph, W., Omenetto, F.G. and Taylor, A.J.: Full-field characterization of femtosecond pulses by spectrum and cross-correlation measurements. *Opt. Lett.*, vol. 24, no. 23, p. 1774, 1999.
Available at: http://dx.doi.org/10.1364/OL.24.001774

[27] Lozovoy, V.V., Xu, B., Coello, Y. and Dantus, M.: Direct measurement of spectral phase for ultrashort laser pulses. *Opt. Express*, vol. 16, no. 2, p. 592, 2008.
Available at: http://dx.doi.org/10.1364/OE.16.000592

[28] Bowlan, P., Gabolde, P., Coughlan, M.A., Trebino, R. and Levis, R.J.: Measuring the spatiotemporal electric field of ultrashort pulses with high spatial and spectral resolution. *Journal of the Optical Society of America B*, vol. 25, no. 6, p. A81, May 2008.
Available at: http://dx.doi.org/10.1364/JOSAB.25.000A81

[29] Galler, A. and Feurer, T.: Pulse shaper assisted short laser pulse characterization. *Applied Physics B*, vol. 90, no. 3-4, pp. 427–430, Mar 2008.
Available at: http://dx.doi.org/10.1007/s00340-007-2924-z

[30] Goodman, J.W.: *Introduction to Fourier Optics*. Roberts & Company, 2005.

[31] Born, M., Wolf, E., Bhatia, A., Gabor, D., Stokes, A., Taylor, A., Wayman, P. and Wilcock, W.: *Principles of Optics: Electromagnetic Theory of Propagation, Interference and Diffraction of Light*. Cambridge University Press, 2000. ISBN 9780521784498.
Available at: http://books.google.co.za/books?id=oV8OAAAAIAAJ

[32] Carlson, F.: *Introduction to applied optics for engineers*. Academic Press, New York, 1977. ISBN 0-12-160050-5.

[33] Hecht, E.: *Optics*. World Student Series, 3rd edn. Addison-Wesley, Reading, Mass., 1998. ISBN 0-201-30425-2.

[34] Silver, S.: Microwave aperture antennas and diffraction theory. *J. Opt. Soc. Am.*, vol. 52, no. 2, p. 131, 1962.
Available at: http://dx.doi.org/10.1364/JOSA.52.000131

[35] Desbois, J., Gires, F. and Turnois, P.: A new approach to picosecond laser pulse analysis shaping and coding. *IEEE J. Quantum Electron.*, vol. 9, no. 2, pp. 213–218, Feb 1973.
Available at: http://dx.doi.org/10.1109/jqe.1973.1077462

[36] Heritage, J.P., Weiner, A.M. and Thurston, R.N.: Picosecond pulse shaping by spectral phase and amplitude manipulation. *Optics Letters*, vol. 10, no. 12, p. 609, Dec 1985.
Available at: http://dx.doi.org/10.1364/OL.10.000609

[37] Weiner, A.M., Heritage, J. and Kirschner, E.M.: High-resolution femtosecond pulse shaping. *Journal of the Optical Society of America B*, vol. 5, no. 8, pp. 1563–1572, Aug 1988.
Available at: http://dx.doi.org/10.1364/JOSAB.5.001563

[38] Weiner, A.M., Leaird, D.E., Patel, J.S. and Wullert, J.R.: Programmable femtosecond pulse shaping by use of a multielement liquid-crystal phase modulator. *Optics Letters*, vol. 15, no. 6, pp. 326–328, Mar 1990.
Available at: `http://dx.doi.org/10.1364/OL.15.000326`

[39] Weiner, A.M., Leaird, D.E., Patel, J. and Wullert, II, J.R.: Programmable shaping of femtosecond optical pulses by use of 128-element liquid crystal phase modulator. *Journal of quantum electronics*, vol. 28, no. 4, pp. 908–920, Apr 1992.
Available at: `http://dx.doi.org/10.1109/3.135209`

[40] Weiner, A.M.: Femtosecond pulse shaping using spatial light modulators. *Review of Scientific Instruments*, vol. 71, no. 5, pp. 1929–1960, 2000.
Available at: `http://dx.doi.org/10.1063/1.1150614`

[41] Weiner, A.M.: Ultrafast optical pulse shaping: A tutorial review. *Optics Communications*, vol. 284, no. 15, pp. 3669–3692, Jul 2011.
Available at: `http://dx.doi.org/10.1016/j.optcom.2011.03.084`

[42] Vaughan, J.C., Hornung, T., Feurer, T. and Nelson, K.A.: Diffraction-based femtosecond pulse shaping with a two-dimensional spatial light modulator. *Optics Letters*, vol. 30, no. 3, p. 323, Feb 2005.
Available at: `http://dx.doi.org/10.1364/OL.30.000323`

[43] Akturk, S., Gu, X., Gabolde, P. and Trebino, R.: The general theory of first-order spatio-temporal distortions of gaussian pulses and beams. *Optics Express*, vol. 13, no. 21, pp. 8642–8661, 2005.
Available at: `http://dx.doi.org/10.1364/OPEX.13.008642`

[44] Brinks, D., Hildner, R., Stefani, F.D. and van Hulst, N.F.: Beating spatio-temporal coupling: implications for pulse shaping and coherent control experiments. *Optics Express*, vol. 19, no. 27, p. 26486, Dec 2011.
Available at: `http://dx.doi.org/10.1364/OE.19.026486`

[45] Frei, F., Bloch, R. and Feurer, T.: Influence of finite spatial resolution on single- and double-pass femtosecond pulse shapers. *Optics Letters*, vol. 35, no. 23, p. 4072, Nov 2010.
Available at: `http://dx.doi.org/10.1364/OL.35.004072`

[46] Frei, F., Galler, A. and Feurer, T.: Space-time coupling in femtosecond pulse shaping and its effects on coherent control. *The Journal of Chemical Physics*, vol. 130, no. 3, p. 034302, 2009.
Available at: `http://dx.doi.org/10.1063/1.3058478`

[47] New, G.: *Introduction to nonlinear optics*. Cambridge University Press, Cambridge New York, 2011. ISBN 0521877016.

[48] Demtröder, W.: *Laser Spectroscopy: Basic Concepts and Instrumentation*. No. v.2 in Advanced Texts in Physics. Springer, 1996. ISBN 9783540571711.

[49] Faulkner, H. and Rodenburg, J.: Error tolerance of an iterative phase retrieval algorithm for moveable illumination microscopy. *Ultramicroscopy*, vol. 103, no. 2, pp. 153–164, may 2005.
Available at: `http://dx.doi.org/10.1016/j.ultramic.2004.11.006`

[50] Vaughan, J.C.: *Two-Dimensional Ultrafast Pulse Shaping and its Application to Coherent Control and Spectroscopy*. Ph.D. thesis, Massachusetts Institute of Technology, 2005.

[51] Treacy, E.B.: Optical pulse compression with diffraction gratings. *IEEE Journal of Quantum Electronics*, vol. 5, no. 9, pp. 454–458, Sep 1969.
Available at: `http://dx.doi.org/10.1109/JQE.1969.1076303`

[52] Martinez, O.E.: Grating and prism compressors in the case of finite beam size. *Journal of the Optical Society of America B*, vol. 3, no. 7, p. 929, Jul 1986.
Available at: `http://dx.doi.org/10.1364/JOSAB.3.000929`

[53] Dudley, A.: *SUPERPOSITIONS OF LIGHT FIELDS CARRYING ORBITAL ANGULAR MOMENTUM*. Ph.D. thesis, University of Kwazulu-Natal, 2012.

[54] Martinez, O., Gordon, J. and Fork, R.: Negative group-velocity dispersion using refraction. *Journal of the Optical Society of America A*, vol. 1, no. 10, pp. 1003–1006, Oct 1984.
Available at: `http://dx.doi.org/10.1364/JOSAA.1.001003`

[55] Ding, Y., Decker, F.-J., Emma, P., Feng, C., Field, C., Frisch, J., Huang, Z., Krzywinski, J., Loos, H., Welch, J., Wu, J. and Zhou, F.: Femtosecond x-ray pulse characterization in free-electron lasers using a cross-correlation technique. *Phys. Rev. Lett.*, vol. 109, p. 254802, Dec 2012.
Available at: `http://link.aps.org/doi/10.1103/PhysRevLett.109.254802`